

Generalized beam model for the analysis of wave propagation with a symmetric pattern of deformation in planar pantographic sheets

Alessandro Ciallella, Ivan Giorgio, Simon R. Eugster, Nicola L. Rizzi,
Francesco dell'Isola

A. Ciallella – DEPARTMENT OF CIVIL, CONSTRUCTION–ARCHITECTURAL AND ENVIRONMENTAL ENGINEERING, University of L'Aquila, Italy

I. Giorgio (Corresponding author) – DEPARTMENT OF CIVIL, CONSTRUCTION–ARCHITECTURAL AND ENVIRONMENTAL ENGINEERING, University of L'Aquila, Italy

E-mail address of corresponding author: ivan.giorgio@univaq.it

S. R. Eugster – INSTITUTE FOR NONLINEAR MECHANICS, University of Stuttgart, Stuttgart, Germany

N. L. Rizzi – DEPARTMENT OF ARCHITECTURE, Roma Tre University, Rome, Italy

F. dell'Isola – DEPARTMENT OF CIVIL, CONSTRUCTION–ARCHITECTURAL AND ENVIRONMENTAL ENGINEERING, University of L'Aquila, Italy

Abstract

Dynamics of pantographic sheets presents exotic aspects that deserve investigation. In this paper, we focus the attention on some possible modalities of non-linear wave propagation in planar pantographic sheets. We use a smaller length-scale lattice model, in which the beams and pivots constituting the sheet are described by constrained Euler–Bernoulli beams together with a meso-reduced-order model which belongs to the class of second-gradient elastic materials and with a macro multi-field 1D continuum model, whose displacement is augmented by a specific class of cross-section deformations. Such a three-step reduction process is developed to allow for fast computational analysis of symmetric wave propagation patterns with respect to the longitudinal axis of the sheet. It is conceived by using suitable kinematical hypotheses for the 1D continuum descriptors referring to pantographic sheet sections which are inspired by the numerical evidence obtained performing simulations based on the smaller scale lattice model. The deformation energy of the pantographic sheet, successfully postulated in [“Large deformations of planar extensible beams and pantographic lattices: heuristic homogenization, experimental and numerical examples of equilibrium”, Proc. R. Soc. A 472: 20150790, 2016] for a meso-reduced-order second gradient model, is pivotal in the whole model reduction process: It allows for the determination of generalized 1D deformation energy in terms of the mechanical properties of the micro-lattice model. Performed numerical simulations prove that

several waveforms propagate in planar pantographic sheets with low dispersion and motivate further investigations in the subject.

Keywords: nonlinear wave propagation, metamaterials, second gradient materials, reduced order model

1 Introduction

In recent literature a great attention is being dedicated to the study of the specific class of mechanical metamaterials [11, 17, 21, 52, 75, 78, 88, 89] called “pantographic materials”.

A pantographic sheet is a structure composed of two layers, each consisting of parallel fibers. These layers lie on top of each other and are oriented such that the fibers intersect, in the top view, typically with an angle of 90 degrees (see, for some different geometries [39, 86]). At every intersection, the fibers of the upper and lower layers are connected either by perfect cylindrical hinges or deformable pivots see Figure 1(a) and (b), respectively.

The pantographic sheet is a material that consists of three different length scales. There is the length scale of the length of the fibers, the scale of the distance between the fibers and the lowest scale, which is determined by the thickness of the fibers and pivots. From a geometrical and kinetical point of view, they bear a remarkable resemblance to the woven fabrics. Indeed, many aspects of the modeling developed for these last can also be adapted for pantographic sheets [79, 80, 92]. Its micro-architecture was conceived, at first, (see [3]) in order to find the synthesis of a 1D continuum generalizing Euler–Bernoulli beam model, whose deformation energy depends also on the gradient of axial elongation. Subsequently, by introducing a multi-scale micro-architecture, pantographic micro-structure was exploited to synthesize 1D continua whose deformation energy depends on the third gradient of transverse displacement (see [69]) or to synthesize plates whose deformation energy depends on the second-gradient of displacements parallel to the plate (see [5]). A rather complete list of the results obtained up to now in the study of pantographic materials can be found in [26, 27, 47], where all their understood exotic mechanical properties are analyzed and a set of interesting open problems is displayed.

In fact, the mechanical behavior of pantographic sheets presents several really exotic aspects and seems to deserve interest by it-self: pantographic materials are extremely damage and failure resistant (see, e.g., [25]) and could be of use in applications where material resilience must be coupled with low weight. Moreover, due to the pantographic substructure, some mode conversions from longitudinal to transverse waves and vice versa may arise. Specifically, when the boundary excitation is purely longitudinal, it is expected that both longitudinal and transverse waves will be generated in the body. This aspect has some similarities with microstructured media of granular motifs (see, e.g., [51, 54, 55]).

However, more generally, it has to be remarked that the pantographic architecture may be considered as a kind of “fundamental brick” to be used to synthesize a rather large class of metamaterials, (see, e.g., [6–8, 87]) and therefore they play a relevant role in the framework of the more general problem of metamaterials synthesis.

In the present paper, we continue the analysis of wave propagation in planar pantographic sheets which was started in [23] and, by using appropriate model reduction techniques and suitably designed numerical integration schemes, we find that interesting waves propagate in non-linear regimes with a slowly changing shape over time.

In our investigations an extensive parametric analysis is necessary: therefore, because of the geometrical and mechanical complexity of pantographic sheets, it is not appropriate to use too detailed models in exploring parametrically the non-linear wave propagation phenomena occurring in them using numerical methods. Therefore, we completely refrained to try to study their dynamics by using those very small length-scale models in which the beams and pivots constituting the sheet are described as 3D Cauchy continua whose reference configuration is the union of cylinders (i.e., elastic pivots) and prisms (i.e., elastic beams) (see Figure 1(b)). Such a modeling choice would imply the solution of non-linear evolutionary problems in which several millions of degrees of freedom are involved, as a detailed mesh is required to account for the deformation of elastic pivots: it is, in fact, well-known that (see [38]) in pantographic sheets a large amount of deformation energy is concentrated in the small volume occupied by the elastic pivots. Moreover, in presence of perfect pivots interconnecting the arrays of beams constituting the sheet, the friction phenomena between the surfaces in contact (Fig. 1(a)), would involve complex coding and the use of unilateral constraints integration schemes: circumstance which may render very difficult the computations with present computing tools, as in every perfect pivot one would have to compute Lagrange multipliers related to constraints represented by inequalities [53, 63].

Instead, in order to perform a faster computational analysis of axisymmetric waves, we propose a generalized 1D continuum model, in which the list of kinematical descriptors include the axial displacement together with a specific set of fields introduced to describe cross-section deformations. The choice of these further kinematical descriptors is made with a judicious conjecture guided by the results obtained using a model where pantographic sheets are described by two arrays of Euler–Bernoulli beams interconnected by cylindrical elastic pivots (see Figure 1(b)), as done in [32]: this last model has a characteristic length-scale greater than the one which is involved in the previously mentioned model based on 3D Cauchy continua. Albeit the computational complexity of this simplified model is smaller compared with 3D continua modeling, it still requires large computing resources and a long computing time: the parametric analysis which we intend to carry out con-

tinues not to be feasible. However, such a beam lattice model can be used for further guiding our model reduction process: i) in allowing for the identification of the constitutive parameters of a second-gradient 2D continuum model (see [1, 10, 59–61, 84, 90]) and ii) in providing the numerical evidence needed to guide the final reduction from the obtained second-gradient 2D continuum model to a 1D generalized continuum model, in which the pantographic planar sheet is modeled as a generalized beam (in the same sense as reported, e.g., in [57, 81]).

In fact, the extra kinematical descriptors which are needed to complement the generalized beam displacement field must be able to describe in a sufficiently detailed way the transverse section deformation (see Fig. 4) in the considered axisymmetric waves so that the identification between the kinematics of the 1D generalized continuum and that of the 2D second-gradient continuum can be obtained efficiently via a kind of Galerkin–Ritz representation i.e, the kinematical micro-macro identification which consists in assuming the existence of continuous macro-fields whose values in designated points allows for the determination of the corresponding micro-kinematical fields.

Once the choice of the kinematical descriptors, on the basis of the aforementioned numerical evidence for the searched 1D generalized continuum is made, then its deformation and kinetic energy are calculated by using Galerkin–Ritz representation and the expression for deformation energy already obtained for the 2D second-gradient continuum model (see [24]). The obtained deformation energy for the final 1D reduced model is used, together with the least action principle, to get an algorithm for calculating numerically its evolution given suitable initial and boundary conditions.

The just described model reduction procedure for considered metamaterial structure is described in detail in the following sections. More precisely, in sect. 2, the first considered model for pantographic sheets is shortly presented: we introduce two arrays of Euler–Bernoulli beams and assume that they are interconnected by perfect cylindrical pivots behaving as constraints. The kinetic energy for such model is postulated simply assuming that the mass density is uniformly distributed along the beams. Some meaningful images taken from numerical simulations are presented, which will suggest the kinematical assumption made in sect. 4. In sect. 3, the intermediate length scale model is introduced and the second-gradient model for pantographic sheet, first introduced in [24], is shortly recalled, by adapting it to the present analysis. In sect. 4, the 1D continuum model is introduced by considering a set of kinematical descriptors suitable for describing axisymmetric non-linear waves in pantographic sheets. In sect. 5, the results of a parametric numerical study are presented. In sect. 6, concluding remarks are formulated to motivate the need of deeper investigations in both theoretical and numerical aspects of the considered problem. An urge for designing experimental set-ups is also raised, giving some hints on how they should be

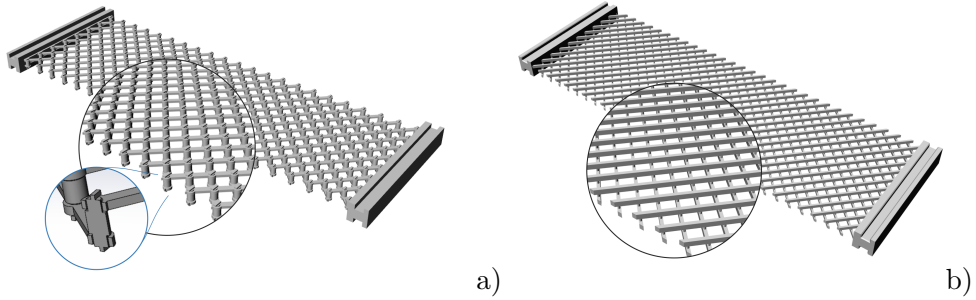


Figure 1: Pantograph with (a) and without (b) perfect pivots. In the second zoom (a), a cutaway diagram of the pivot.

designed [5, 6, 34, 35].

2 The planar beam lattice model for pantographic sheets

To eliminate the lowest scale, the pantographic sheet can be modeled as an assembly of interconnected planar nonlinear beams, which are planar curves with elastic resistance against stretching and flexure as well as a homogeneous mass density per unit length. In the following, we briefly describe the model that was introduced in [32].

The pantographic sheet with length L and height B is composed of n_{row} rows and n_{col} columns of straight beams each of which has a reference length of $l = \sqrt{2}B/n_{\text{row}}$. In total there are $n_b = n_{\text{row}}n_{\text{col}}$ individual beams. All beams are modeled as Euler–Bernoulli beams discretized with B-spline shape functions as discussed in [43]. Hence, the centerline position of beam $b \in \{1, \dots, n_b\}$ is approximated by the function $\mathbf{r}(s, \mathbf{q}_b(t)) = \mathbf{N}(s)\mathbf{q}_b(t) \in \mathbb{R}^2$, where s denotes the referential arc-length, $\mathbf{q}_b = \mathbf{q}_b(t) \in \mathbb{R}^{2n_c}$ is the vector consisting of the coordinates of the n_{cp} control points and $\mathbf{N} = \mathbf{N}(s) \in \mathbb{R}^{2 \times 2n_{\text{cp}}}$ is the matrix of B-spline basis functions. These interpolation functions characterize numerical codes based on isogeometric analysis (see, e.g., [15, 16, 40–42, 49, 56, 83, 91] for more details). Using a Bubnov–Galerkin approximation procedure of the Euler–Bernoulli beam, the internal virtual work of an individual beam can be approximated as

$$\begin{aligned} \delta W_b^{\text{int,h}} &= \delta \mathbf{q}_b(t)^\top \mathbf{f}_b^{\text{int}}(\mathbf{q}_b), \\ \mathbf{f}_b^{\text{int}} &= - \int_0^l \left\{ \frac{1}{g} \mathbf{N}'^\top \left(\mathbf{r}' N - \frac{M}{g} [2\theta' \mathbf{r}' + \mathbf{r}'_\perp] \right) + \mathbf{N}''^\top \mathbf{r}'_\perp \frac{M}{g^2} \right\} ds, \end{aligned} \quad (1)$$

where prime denotes the derivative with respect to s , $g = \|\mathbf{r}'\|$, N , M , θ and $\delta \mathbf{q}_b$ are the axial stretch, the axial force, the bending couple, the inclination angle, and the virtual displacements of the control point positions,

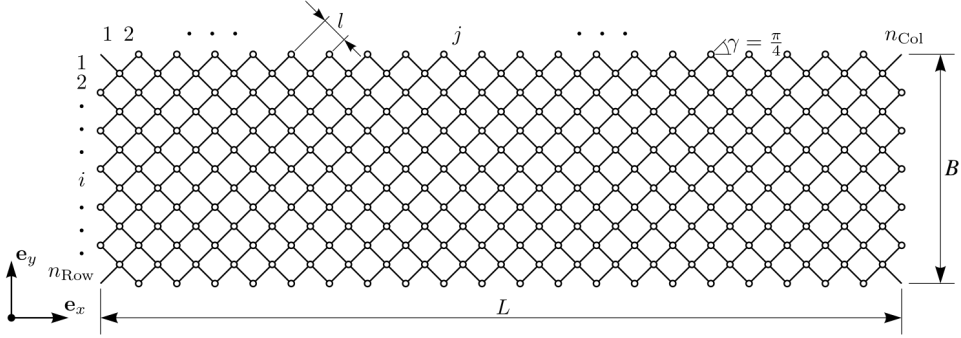


Figure 2: Scheme of pantograph with perfect pivots in the reference configuration.

respectively. Moreover, we have made use of the mapping

$$\perp : \mathbf{a} = (a_1, a_2) \mapsto \mathbf{a}_\perp = (-a_2, a_1). \quad (2)$$

The axial force and the bending couple are related to the axial stretch and the change in inclination angle, i.e., the curvature, $\theta' = (\mathbf{r}'_\perp)^\top \mathbf{r}'' g^{-2}$ by the linear constitutive laws $N = k_e(g - 1)$ and $M = k_b \theta'$, where k_e and k_b are the respective axial and bending stiffnesses. Neglecting the cross-section inertia of the beam, only the mass concentrated on the centerline is taken into account and leads after the discretization to the inertial virtual work functional

$$\delta W_b^{\text{dyn,h}} = -\delta \mathbf{q}_b(t)^\top \mathbf{M}_b \ddot{\mathbf{q}}_b(t), \quad \mathbf{M}_b = \int_0^l A_{\rho_0} \mathbf{N}^\top \mathbf{N} ds, \quad (3)$$

where \mathbf{M}_b is the constant, symmetric and positive definite mass matrix of the discretized beam. The generalized coordinates $\mathbf{q} = (\mathbf{q}_1, \dots, \mathbf{q}_{n_b})$ of the entire pantographic sheet are the position coordinates of the control points of all individual beams. We introduce the Boolean matrix \mathbf{C}_b in order to extract the beam coordinates from \mathbf{q} in agreement with $\mathbf{q}_b = \mathbf{C}_b \mathbf{q}$.

The model is completed by the interaction between the individual beams and the environment both of which are taken into account by adding perfect bilateral constraints. The possibly time dependent constraint conditions $\mathbf{g}(\mathbf{q}, t) = 0$ are determined from the following requirements and can be found in detail in [32]. For a more general insight about this critical topic, see [14].

- (i) Within a single beam family, at the connection points, two adjacent beams must agree on their position and inclination angle.
- (ii) At the intersection of the two fiber families, the corresponding beams must have the same position throughout the motion.
- (iii) The chosen boundary conditions dictate the e_x -coordinates of the points at the left and right edge of the pantograph. Specifically, the

e_x -coordinates of the left boundary points are given by the excitation function $e(t)$, the e_x -coordinates of the right boundary points are blocked. Both the e_y -coordinates of the left and right boundary are allowed to move freely.

The total virtual work functional of the entire discretized pantograph is then given by

$$\delta W^{\text{tot}} = -\delta \mathbf{q}^\top \left(\mathbf{M}\ddot{\mathbf{q}} - \mathbf{h}(\mathbf{q}) - \left(\frac{\partial \mathbf{g}}{\partial \mathbf{q}}(\mathbf{q}, t) \right)^\top \boldsymbol{\lambda} \right), \quad (4)$$

with the constant, symmetric, and positive definite mass matrix

$$\mathbf{M} = \sum_{b=1}^{n_b} \mathbf{C}_b^\top \mathbf{M}_b \mathbf{C}_b, \quad (5)$$

and the generalized forces of all n_b beams

$$\mathbf{h}(\mathbf{q}) = \sum_{b=1}^{n_b} \mathbf{C}_b^\top \mathbf{f}_b^{\text{int}}(\mathbf{C}_b \mathbf{q}). \quad (6)$$

The Lagrange multipliers $\boldsymbol{\lambda}$ are the constraint forces that enforce the constraint conditions $\mathbf{g}(\mathbf{q}, t) = 0$. Since by the principle of virtual work, for each time instant t , the virtual work must vanish, the discretized pantographic sheet is described by the differential algebraic system of equations

$$\begin{aligned} \mathbf{M}\ddot{\mathbf{q}} - \mathbf{h}(\mathbf{q}) - \mathbf{W}(\mathbf{q}, t)\boldsymbol{\lambda} &= 0, \\ \mathbf{g}(\mathbf{q}, t) &= 0. \end{aligned} \quad (7)$$

For the numerical time integration of (7), we used the generalized- α scheme for constrained mechanical systems of index 3 proposed by [4].

As excitation functions, we chose

$$\begin{aligned} e_1(t) &= \frac{e_0}{2} \tanh \left[\frac{4(t - s_1)}{s_1} \right] + \frac{e_0}{2} \tanh(4), \\ e_2(t) &= e_0 \sin \left(\frac{n\pi}{2s_1} t \right) [S_{1,[0,s_1]}(t) - S_{1,[s_1,2s_1]}(t)], \end{aligned} \quad (8)$$

where for the latter function the first smooth step function S_{1,I_1} for the interval $I_1 = [a, b]$ is required. This is defined as

$$S_{1,[a,b]}(t) = \begin{cases} 0 & t < a, \\ -2 \left(\frac{t-a}{b-a} \right)^3 + 3 \left(\frac{t-a}{b-a} \right)^2 & a \leq t \leq b, \\ 1 & b < t. \end{cases} \quad (9)$$

In Figure 3, the e_y -displacements of a simulation with the parameters from Table 1 are shown. The required simulation time was around 4 hours

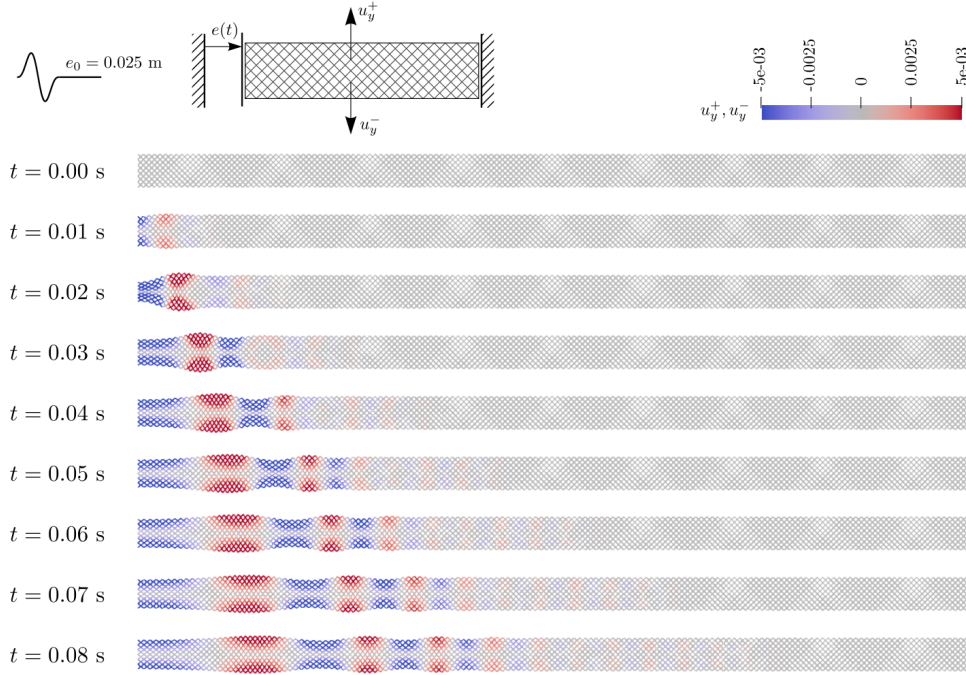


Figure 3: Excitation with $e = e_2$, $s_1 = 0.01$ s and $e_0 = 0.025$ m.

geometric properties		kinetic properties	
n_{row}	12	k_e	500 N
n_{col}	300	k_b	$417 \times 10^{-7} \text{ Nm}^2$
B	$n_{\text{row}} \times 0.01$ m	A_{ρ_0}	$94 \times 10^{-5} \text{ kgm}^{-1}$
L	$n_{\text{col}} \times 0.01$ m		
spatial discretization		time discretization	
# el./beam	1	t_e	8×10^{-2} s
polynomial degree	3	Δt	2×10^{-5} s
# quadr. points/el.	5	ρ_∞	0.8

Table 1: Model and discretization parameters.

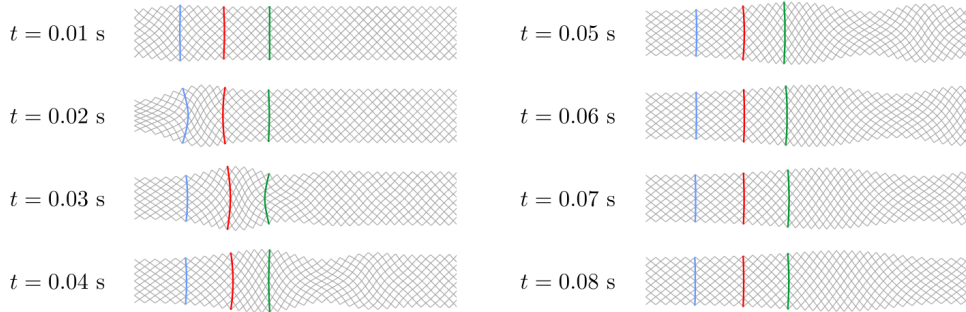


Figure 4: Close-up of longitudinal wave propagation from Figure 3. The transverse section deformation is highlighted for $j = \{10, 20, 30\}$ in blue, red and green.

on a standard desktop computer with a numerical code implemented in Python 3. For a reasonable parametric study a reduction by a factor of 100 or more would be desirable. There are two ways to achieve this. The first non-mechanical solution is to implement the system dynamics in a faster programming language like C++ or Fortran and to exploit possible parallelization procedures. The second solution lies in a further scale reduction, which requires further mechanical modeling. Aiming for a reduction that captures the axisymmetric dynamic behavior of the pantographic sheet as a one-dimensional generalized continuum, the main features of non-linear waves revealed in the numerical analysis of the pantographic sheet in Figure 3 are:

- (i) a concentration of the support of some propagating wave packages, albeit their dispersion;
- (ii) wave shapes that seem to have the tendency to change slowly during propagation;
- (iii) the presence of typical deformation patterns of the transverse sections as highlighted in Figure 4.

3 Second-gradient planar continuum for pantographic sheet

The detailed model presented in the previous section could give us some important information about the dynamic behavior of planar pantographic sheets. However, its ability to give some rigorous qualitative results about the possibility of observing some solitary-type waves propagating is restrained by a huge computational burden. A main conceptual effort in order to construct a further reduced model seems demanded and it is the matter of the present and the next sections. Following the procedure leading to the formal asymptotic expansion presented in [24] a second-gradient continuum model for pantographic sheets can be obtained, whose properties have been extensively explored: such model has revealed a remarkable predictive capacity when static deformation phenomena are considered (see e.g. [19, 22, 26–29, 31, 76, 77]). It is therefore reasonable to assume that, once complemented with the kinetic energy associated to the motion of the involved arrays of beams, the second gradient deformation energy deduced there can give a reliable basis, via the least action principle, to describe the motion at the chosen length-scale (some results available in the literature for the dynamics regime on generalized continuum models could be found in, e.g., [2, 9, 13, 30, 62, 68, 72, 74, 85]). This length-scale is greater than the distance between the closest interconnecting pivots, while the previous lattice beam model has as characteristic length-scale the one of the beams sections diameters.

We remark that a second gradient continuum model falls in the category of materials characterized by non-local interactions, as may happen when additional kinematical descriptors are added to the formulation with some internal constraints [33,46,50,82]. Similar interactions are taken into account in peridynamic models, where a long-range interaction within a horizon radius is considered [20,36,45,58].

In the second-gradient model that we shortly describe here, the material points in the reference configuration $\Omega \subset \mathbb{E}^3$ are labelled by

$$\mathbf{X} = X_1 \mathbf{E}_1 + X_2 \mathbf{E}_2 = \xi_1 \mathbf{D}_1 + \xi_2 \mathbf{D}_2, \quad (10)$$

where $(X_1, X_2) \in \mathbb{R}^2$ and $(\xi_1, \xi_2) \in \mathbb{R}^2$ are the Cartesian coordinates sharing the same origin \mathcal{O} and with orthonormal bases $\{\mathbf{E}_1, \mathbf{E}_2\}$ and $\{\mathbf{D}_1, \mathbf{D}_2\}$, respectively (see Fig. 5).

While the \mathbf{E}_i -basis corresponds with the direction of the edges of the pantographic sheet where we search for some propagating non-linear waves, the \mathbf{D}_i -basis, which is rotated with respect to \mathbf{E}_i by $\pi/4$ in clockwise direction, gives the two pantographic fiber directions of the sheet, see Fig. 5. Accordingly, for $\alpha \in \{1, 2\}$, the two associated Cartesian coordinates are related by the relationship:

$$X_1(\xi_1, \xi_2) = \frac{\sqrt{2}}{2} \xi_1 + \frac{\sqrt{2}}{2} \xi_2, \quad X_2(\xi_1, \xi_2) = -\frac{\sqrt{2}}{2} \xi_1 + \frac{\sqrt{2}}{2} \xi_2. \quad (11)$$

For coinciding current and referential base vectors, i.e., $\mathbf{e}_i = \mathbf{E}_i$, we will look for waves for which the motion of the pantographic sheet is more suitably expressed in X -coordinates as follows:

$$\boldsymbol{\chi} = \boldsymbol{\chi}(X_1, X_2, t) = \chi_1(X_1, X_2, t) \mathbf{E}_1 + \chi_2(X_1, X_2, t) \mathbf{E}_2.$$

In what follows, when this will not cause misunderstandings, we will mostly omit the explicit indication of the t dependence. Instead, to formulate in terms of placement field the strain energy density, it is convenient to represent the motion also in the ξ -coordinates, as follows:

$$\tilde{\boldsymbol{\chi}}(\xi_1, \xi_2) = \boldsymbol{\chi}(X_1(\xi_1, \xi_2), X_2(\xi_1, \xi_2)). \quad (12)$$

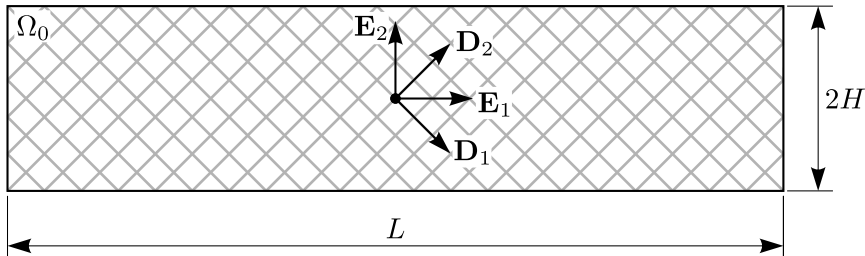


Figure 5: Reference configuration of the pantographic sheet.

Let us consider a position $\mathbf{P} \equiv (X_1, X_2)$ in the reference configuration and the two functions

$$\begin{aligned}\tilde{\chi}_1 &= \tilde{\chi}(\cdot, \xi_2) = \chi(X_1(\cdot, \xi_2), X_2(\cdot, \xi_2)) \\ \tilde{\chi}_2 &= \tilde{\chi}(\xi_1, \cdot) = \chi(X_1(\xi_1, \cdot), X_2(\xi_1, \cdot))\end{aligned}\quad (13)$$

where $\tilde{\chi}_1$ and $\tilde{\chi}_2$ are the shapes under $\tilde{\chi}$ of the coordinate lines passing through \mathbf{P} and parallel to \mathbf{D}_1 and \mathbf{D}_2 , respectively.

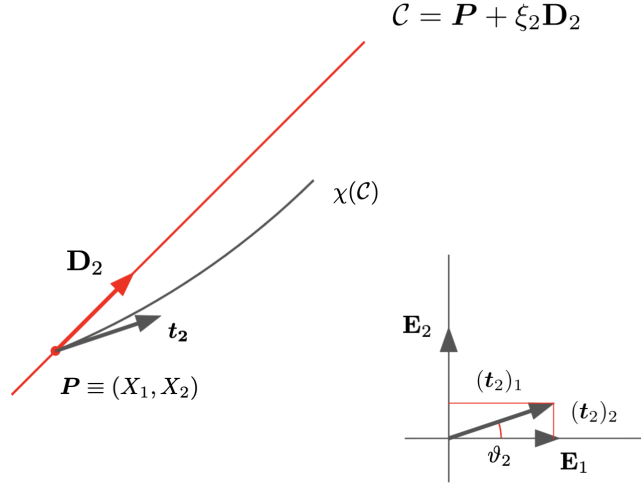


Figure 6: Shape of a fiber trough P along \mathbf{D}_2 in the reference and present configuration.

With reference to $\tilde{\chi}_2$ (see Fig. 6) we can define: *i*) the unit tangent field; *ii*) the unit normal field; *iii*) the curvature field. The tangent to $\tilde{\chi}(\mathcal{C})$ at \mathbf{P} is

$$\mathbf{t}_2 = \frac{\partial \tilde{\chi}_2}{\partial \xi_2} \quad (14)$$

while its length is

$$\rho_2 = \|\mathbf{t}_2\| = \left\| \frac{\partial \tilde{\chi}_2}{\partial \xi_2} \right\| \quad (15)$$

The vector \mathbf{t}_2 can be written as (see Fig. 6)

$$\mathbf{t}_2 = \rho_2(\cos \vartheta_2 \mathbf{E}_1 + \sin \vartheta_2 \mathbf{E}_2) \quad (16)$$

where

$$\vartheta_2 = \arctan \frac{(\mathbf{t}_2)_2}{(\mathbf{t}_2)_1} \quad (17)$$

The unit tangent vector reads

$$\tilde{\mathbf{t}}_2 = \frac{\mathbf{t}_2}{\|\mathbf{t}_2\|} = \cos \vartheta_2 \mathbf{E}_1 + \sin \vartheta_2 \mathbf{E}_2 \quad (18)$$

and the normal vector is

$$\mathbf{n}_2 = \frac{\tilde{\mathbf{t}}_2}{\partial \xi_2} = (-\sin \vartheta_2 \mathbf{E}_1 + \cos \vartheta_2 \mathbf{E}_2) \frac{\partial \vartheta_2}{\partial \xi_2} \quad (19)$$

From (19) can easily be seen that the unit normal vector and the curvature are

$$\begin{aligned} \tilde{\mathbf{n}}_2 &= -\sin \vartheta_2 \mathbf{E}_1 + \cos \vartheta_2 \mathbf{E}_2 \\ c_2 &= \frac{\partial \vartheta_2}{\partial \xi_2} \end{aligned} \quad (20)$$

respectively.

Note that analogous expressions can be written for $\tilde{\chi}_1$ and both can be summarized by the following expressions.

Using the chain rule, the derivative with respect to ξ_α can be written as

$$\begin{aligned} \mathbf{t}_\alpha &= \frac{\partial \tilde{\chi}}{\partial \xi_\alpha} = \frac{\partial \chi}{\partial X_1}(X_1(\cdot), X_2(\cdot)) \frac{\partial X_1}{\partial \xi_\alpha} + \frac{\partial \chi}{\partial X_2}(X_1(\cdot), X_2(\cdot)) \frac{\partial X_2}{\partial \xi_\alpha} \\ &= \frac{\sqrt{2}}{2} \left(\frac{\partial \chi}{\partial X_1}(X_1(\cdot), X_2(\cdot)) + (-1)^\alpha \frac{\partial \chi}{\partial X_2}(X_1(\cdot), X_2(\cdot)) \right). \end{aligned} \quad (21)$$

Similarly, the derivative of \mathbf{t}_α with respect to ξ_α can be easily calculated as follows:

$$\begin{aligned} \frac{\partial \mathbf{t}_\alpha}{\partial \xi_2} &= \frac{\partial^2 \tilde{\chi}}{\partial \xi_\alpha^2} = \frac{\sqrt{2}}{2} \left(\frac{\partial^2 \chi}{\partial X_1^2}(X_1(\cdot), X_2(\cdot)) \frac{\partial X_1}{\partial \xi_\alpha} + \frac{\partial^2 \chi}{\partial X_1 \partial X_2}(X_1(\cdot), X_2(\cdot)) \frac{\partial X_2}{\partial \xi_\alpha} + \right. \\ &\quad \left. + (-1)^\alpha \frac{\partial^2 \chi}{\partial X_2 \partial X_1}(X_1(\cdot), X_2(\cdot)) \frac{\partial X_1}{\partial \xi_\alpha} + (-1)^\alpha \frac{\partial^2 \chi}{\partial X_2^2}(X_1(\cdot), X_2(\cdot)) \frac{\partial X_2}{\partial \xi_\alpha} \right) \\ &= \frac{1}{2} \left(\frac{\partial^2 \chi}{\partial X_1^2} + 2(-1)^\alpha \frac{\partial^2 \chi}{\partial X_1 \partial X_2} + \frac{\partial^2 \chi}{\partial X_2^2} \right) (X_1(\cdot), X_2(\cdot)). \end{aligned} \quad (22)$$

On the other hand, eqn. (21) can be written as

$$\mathbf{t}_\alpha = \frac{\partial \tilde{\chi}}{\partial \xi_\alpha} = \rho_\alpha (\cos(\vartheta_\alpha) \mathbf{E}_1 + \sin(\vartheta_\alpha) \mathbf{E}_2). \quad (23)$$

where

$$\begin{aligned} \rho_\alpha &= \|\mathbf{t}_\alpha\| = \left\| \frac{\partial \tilde{\chi}_\alpha}{\partial \xi_\alpha} \right\| \\ \vartheta_\alpha &= \arctan \left(\frac{t_{\alpha 2}}{t_{\alpha 1}} \right) = \arctan \left(\frac{\frac{\partial \tilde{\chi}}{\partial \xi_\alpha} \cdot \mathbf{E}_2}{\frac{\partial \tilde{\chi}}{\partial \xi_\alpha} \cdot \mathbf{E}_1} \right) \end{aligned} \quad (24)$$

ρ_α and ϑ_α being the fiber stretch and the fiber inclination angle, respectively.

The following fields can be easily derived

$$\begin{aligned}
\tilde{\mathbf{t}}_\alpha &= \cos \vartheta_\alpha \mathbf{E}_1 + \sin \vartheta_\alpha \mathbf{E}_2 \\
\mathbf{n}_\alpha &= \frac{\tilde{\mathbf{t}}_\alpha}{\partial \xi_\alpha} = (-\sin \vartheta_\alpha \mathbf{E}_1 + \cos \vartheta_\alpha \mathbf{E}_2) \frac{\partial \vartheta_\alpha}{\partial \xi_\alpha} \\
\tilde{\mathbf{n}}_\alpha &= -\sin \vartheta_\alpha \mathbf{E}_1 + \cos \vartheta_\alpha \mathbf{E}_2 \\
\mathbf{t}_{\alpha\perp} &= \rho_\alpha \tilde{\mathbf{n}}_\alpha = \rho_\alpha (-\sin \vartheta_\alpha \mathbf{E}_1 + \cos \vartheta_\alpha \mathbf{E}_2)
\end{aligned} \tag{25}$$

where $\tilde{\mathbf{t}}_\alpha$ is the unit tangent vector, \mathbf{n}_α and $\tilde{\mathbf{n}}_\alpha$ are the normal and unit normal vectors, and $\mathbf{t}_{\alpha\perp}$ is obtained by eqn. (2).

Accordingly, the first variation of the stretch is equal to

$$\delta \rho_\alpha = \frac{1}{\rho_\alpha} \frac{\partial \delta \tilde{\chi}}{\partial \xi_\alpha} \cdot \frac{\partial \tilde{\chi}}{\partial \xi_\alpha}. \tag{26}$$

Now, using (23), (22) can be written in the form

$$\begin{aligned}
\frac{\partial \mathbf{t}_\alpha}{\partial \xi_\alpha} &= \frac{\partial^2 \tilde{\chi}}{\partial \xi_\alpha^2} = \frac{\partial \rho_\alpha}{\partial \xi_\alpha} [\cos(\vartheta_\alpha) \mathbf{E}_1 + \sin(\vartheta_\alpha) \mathbf{E}_2] + \frac{\partial \vartheta_\alpha}{\partial \xi_\alpha} \rho_\alpha [-\sin(\vartheta_\alpha) \mathbf{E}_1 + \cos(\vartheta_\alpha) \mathbf{E}_2] \\
&= \frac{\partial \rho_\alpha}{\partial \xi_\alpha} \tilde{\mathbf{t}}_\alpha + \frac{\partial \vartheta_\alpha}{\partial \xi_\alpha} \rho_\alpha \tilde{\mathbf{n}}_\alpha
\end{aligned} \tag{27}$$

It readily follows that the curvature of the α -fiber is obtained as

$$\frac{\partial \vartheta_\alpha}{\partial \xi_\alpha} = \frac{1}{\rho_\alpha^2} \left(\frac{\partial \tilde{\chi}}{\partial \xi_\alpha} \right)_\perp \cdot \frac{\partial^2 \tilde{\chi}}{\partial \xi_\alpha^2} = \frac{1}{\rho_\alpha^2} \frac{\partial \mathbf{t}_\alpha}{\partial \xi_\alpha} \cdot \mathbf{t}_{\alpha\perp} \tag{28}$$

By using (24)₂, we can compute the virtual rotation as

$$\delta \vartheta_\alpha = \frac{1}{\rho_\alpha^2} \mathbf{t}_{\alpha\perp} \cdot \delta \mathbf{t}_\alpha \tag{29}$$

The first variation of the curvature of the α -fiber, and using the relation $\mathbf{a}_\perp \cdot \mathbf{b} = -\mathbf{a} \cdot \mathbf{b}_\perp$ as well as (26) and (28), we obtain

$$\begin{aligned}
\delta \left(\frac{\partial \vartheta_\alpha}{\partial \xi_\alpha} \right) &= -2\rho_\alpha^{-1} \delta \rho_\alpha \frac{1}{\rho_\alpha^2} \left(\frac{\partial \tilde{\chi}}{\partial \xi_\alpha} \right)_\perp \cdot \frac{\partial^2 \tilde{\chi}}{\partial \xi_\alpha^2} + \\
&\quad + \frac{1}{\rho_\alpha^2} \left[\left(\frac{\partial \delta \tilde{\chi}}{\partial \xi_\alpha} \right)_\perp \cdot \frac{\partial^2 \tilde{\chi}}{\partial \xi_\alpha^2} + \left(\frac{\partial \tilde{\chi}}{\partial \xi_\alpha} \right)_\perp \cdot \frac{\partial^2 \delta \tilde{\chi}}{\partial \xi_\alpha^2} \right] \\
&= \frac{1}{\rho_\alpha^2} \left\{ \left(\frac{\partial \tilde{\chi}}{\partial \xi_\alpha} \right)_\perp \cdot \frac{\partial^2 \delta \tilde{\chi}}{\partial \xi_\alpha^2} - \frac{\partial \delta \tilde{\chi}}{\partial \xi_\alpha} \cdot \left[2 \frac{\partial \vartheta_\alpha}{\partial \xi_\alpha} \frac{\partial \tilde{\chi}}{\partial \xi_\alpha} + \left(\frac{\partial^2 \tilde{\chi}}{\partial \xi_\alpha^2} \right)_\perp \right] \right\} \\
&= \frac{1}{\rho_\alpha^2} \left\{ \mathbf{t}_{\alpha\perp} \cdot \frac{\partial \delta \mathbf{t}_\alpha}{\partial \xi_\alpha} - \delta \mathbf{t}_\alpha \cdot \left[2 \frac{\partial \vartheta_\alpha}{\partial \xi_\alpha} \mathbf{t}_\alpha + \left(\frac{\partial \mathbf{t}_\alpha}{\partial \xi_\alpha} \right)_\perp \right] \right\}
\end{aligned} \tag{30}$$

The strain energy of the pantographic sheet without shear rigidity (pivots as perfect hinges) is defined as

$$\Pi^{\text{int}}(\boldsymbol{\chi}) = \int_{-H}^H \int_0^L \sum_{\alpha=1}^2 \left[\frac{1}{2} k_e (\rho_\alpha - 1)^2 + \frac{1}{2} k_b \left(\frac{\partial \vartheta_\alpha}{\partial \xi_\alpha} \right)^2 \right] dX_1 dX_2. \quad (31)$$

By putting $N_\alpha = k_e(\rho_\alpha - 1)$ and $M_\alpha = k_b \partial \vartheta_\alpha / \partial \xi_\alpha$, the internal virtual work is the negative of the strain energies variation, which is

$$\delta W^{\text{int}} = -\delta \Pi^{\text{int}} = - \int_{-H}^H \int_0^L \sum_{\alpha=1}^2 \left[\delta \rho_\alpha N_\alpha + \delta \left(\frac{\partial \vartheta_\alpha}{\partial \xi_\alpha} \right) M_\alpha \right] dX_1 dX_2. \quad (32)$$

Inserting (26) and (30), the internal virtual work can be expressed in terms of the motion as

$$\begin{aligned} \delta W^{\text{int}} &= - \int_{-H}^H \int_0^L \sum_{\alpha=1}^2 \left\{ \frac{\partial \delta \tilde{\boldsymbol{\chi}}}{\partial \xi_\alpha} \cdot \frac{1}{\rho_\alpha} \left(\frac{\partial \tilde{\boldsymbol{\chi}}}{\partial \xi_\alpha} N_\alpha - \frac{M_\alpha}{\rho_\alpha} \left[2 \frac{\partial \vartheta_\alpha}{\partial \xi_\alpha} \frac{\partial \tilde{\boldsymbol{\chi}}}{\partial \xi_\alpha} + \left(\frac{\partial^2 \tilde{\boldsymbol{\chi}}}{\partial \xi_\alpha^2} \right)_\perp \right] \right) \right. \\ &\quad \left. + \frac{\partial^2 \delta \tilde{\boldsymbol{\chi}}}{\partial \xi_\alpha^2} \cdot \left(\frac{\partial \tilde{\boldsymbol{\chi}}}{\partial \xi_\alpha} \right)_\perp \frac{M_\alpha}{\rho_\alpha^2} \right\} dX_1 dX_2 \\ &= - \int_{-H}^H \int_0^L \sum_{\alpha=1}^2 \left\{ \frac{\partial \delta \tilde{\boldsymbol{\chi}}}{\partial \xi_\alpha} \cdot \mathbf{p}_\alpha + \frac{\partial^2 \delta \tilde{\boldsymbol{\chi}}}{\partial \xi_\alpha^2} \cdot \mathbf{m}_\alpha \right\} dX_1 dX_2. \end{aligned} \quad (33)$$

where we have introduced

$$\mathbf{p}_\alpha = \frac{1}{\rho_\alpha} \left(\frac{\partial \tilde{\boldsymbol{\chi}}}{\partial \xi_\alpha} N_\alpha - \frac{M_\alpha}{\rho_\alpha} \left[2 \frac{\partial \vartheta_\alpha}{\partial \xi_\alpha} \frac{\partial \tilde{\boldsymbol{\chi}}}{\partial \xi_\alpha} + \left(\frac{\partial^2 \tilde{\boldsymbol{\chi}}}{\partial \xi_\alpha^2} \right)_\perp \right] \right), \quad (34)$$

$$\mathbf{m}_\alpha = \left(\frac{\partial \tilde{\boldsymbol{\chi}}}{\partial \xi_\alpha} \right)_\perp \frac{M_\alpha}{\rho_\alpha^2}. \quad (35)$$

The kinetic energy of the pantographic sheet can be assumed at the first approximation as

$$K_E(\dot{\boldsymbol{\chi}}) = \int_{-H}^H \int_0^L \frac{1}{2} \varrho_A \dot{\boldsymbol{\chi}} \cdot \dot{\boldsymbol{\chi}} dX_1 dX_2 \quad (36)$$

ϱ_A being the mass density per unit area, assumed in this case uniformly distributed, and neglecting the micro-inertia of the pantographic sub-structure (see for more details [73]).

The response of pantographic sheets presents a hysteretic behavior due to dissipative phenomena [18, 70]; however, in this paper, we neglect this aspect that will be addressed in future works. As a matter of fact, this behavior is rather complex and can derive from diverse sources, such as friction in the case of the perfect pivots, structural dissipation due to the poor quality of 3D printing [64, 71], and some plasticity involved.

4 Generalized 1D continuum model

In order to capture the complex behavior of the pantographic sheet, we make the following reduction Ansatz which is valid for axisymmetric placements

$$\boldsymbol{\chi}(X_1, X_2) = r(X_1)\mathbf{E}_1 + \sum_{i=1}^k a_i(X_1)X_2^{2i}\mathbf{E}_1 + \sum_{j=1}^l b_j(X_1)X_2^{2j-1}\mathbf{E}_2 \quad (37)$$

The three addends can be interpreted respectively as the placement of the centerline of the introduced 1D continuum, as well as the warping and contraction of its cross sections. The undeformed configuration is obtained for

$$\begin{aligned} r(X_1) &= X_1, & a_i(X_1) &= 0 \text{ for } i = 1, \dots, k, \\ b_1(X_1) &= 1, & b_j(X_1) &= 0 \text{ for } j = 2, \dots, l. \end{aligned} \quad (38)$$

For the computation of the stretch and the curvatures, the derivatives up to second order with respect to X_1 and X_2 are required. Denoting with a prime the X_1 -derivatives, they are

$$\begin{aligned} \frac{\partial \boldsymbol{\chi}}{\partial X_1} &= (r' + \sum_{i=1}^k a_i' X_2^{2i})\mathbf{E}_1 + \sum_{j=1}^l b_j' X_2^{2j-1}\mathbf{E}_2 \\ \frac{\partial \boldsymbol{\chi}}{\partial X_2} &= \sum_{i=1}^k 2ia_i X_2^{2i-1}\mathbf{E}_1 + \sum_{j=1}^l (2j-1)b_j X_2^{2j-2}\mathbf{E}_2 \\ \frac{\partial^2 \boldsymbol{\chi}}{\partial X_1^2} &= (r'' + \sum_{i=1}^k a_i'' X_2^{2i})\mathbf{E}_1 + \sum_{j=1}^l b_j'' X_2^{2j-1}\mathbf{E}_2 \\ \frac{\partial^2 \boldsymbol{\chi}}{\partial X_2^2} &= \sum_{i=1}^k 2i(2i-1)a_i X_2^{2i-2}\mathbf{E}_1 + \sum_{j=1}^l (2j-1)(2j-2)b_j X_2^{2j-3}\mathbf{E}_2 \\ \frac{\partial^2 \boldsymbol{\chi}}{\partial X_1 \partial X_2} &= \sum_{i=1}^k 2ia_i' X_2^{2i-1}\mathbf{E}_1 + \sum_{j=1}^l (2j-1)b_j' X_2^{2j-2}\mathbf{E}_2 \end{aligned} \quad (39)$$

The first fiber derivative for the restricted kinematics can be computed by (21) as

$$\begin{aligned} \frac{\partial \tilde{\boldsymbol{\chi}}}{\partial \xi_\alpha} &= \frac{\sqrt{2}}{2} \left(r' + \sum_{i=1}^k [a_i' X_2^{2i} + (-1)^\alpha 2ia_i X_2^{2i-1}] \right) \mathbf{E}_1 \\ &\quad + \frac{\sqrt{2}}{2} \left(\sum_{j=1}^l [b_j' X_2^{2j-1} + (-1)^\alpha (2j-1)b_j X_2^{2j-2}] \right) \mathbf{E}_2, \end{aligned} \quad (40)$$

which using eqn. (2) leads to

$$\begin{aligned} \left(\frac{\partial \tilde{\chi}}{\partial \xi_\alpha} \right)_\perp &= -\frac{\sqrt{2}}{2} \left(\sum_{j=1}^l [b'_j X_2^{2j-1} + (-1)^\alpha (2j-1) b_j X_2^{2j-2}] \right) \mathbf{E}_1 \\ &+ \frac{\sqrt{2}}{2} \left(r' + \sum_{i=1}^k [a'_i X_2^{2i} + (-1)^\alpha 2i a_i X_2^{2i-1}] \right) \mathbf{E}_2 . \end{aligned} \quad (41)$$

The variation of (40) is then

$$\begin{aligned} \frac{\partial \delta \tilde{\chi}}{\partial \xi_\alpha} &= \frac{\sqrt{2}}{2} \left(\delta r' + \sum_{i=1}^k [\delta a'_i X_2^{2i} + (-1)^\alpha 2i \delta a_i X_2^{2i-1}] \right) \mathbf{E}_1 \\ &+ \frac{\sqrt{2}}{2} \left(\sum_{j=1}^l [\delta b'_j X_2^{2j-1} + (-1)^\alpha (2j-1) \delta b_j X_2^{2j-2}] \right) \mathbf{E}_2 , \end{aligned} \quad (42)$$

The second derivative in fiber direction is computed in accordance with (22) as

$$\begin{aligned} \frac{\partial^2 \tilde{\chi}}{\partial \xi_\alpha^2} &= \frac{1}{2} \left(r'' + \sum_{i=1}^k [a''_i X_2^{2i} + 2(-1)^\alpha 2i a'_i X_2^{2i-1} + 2i(2i-1) a_i X_2^{2i-2}] \right) \mathbf{E}_1 \\ &+ \frac{1}{2} \left(\sum_{j=1}^l [b''_j X_2^{2j-1} + 2(-1)^\alpha (2j-1) b'_j X_2^{2j-2} + (2j-1)(2j-2) b_j X_2^{2j-3}] \right) \mathbf{E}_2 . \end{aligned} \quad (43)$$

and

$$\begin{aligned} \left(\frac{\partial^2 \tilde{\chi}}{\partial \xi_\alpha^2} \right)_\perp &= -\frac{1}{2} \left(\sum_{j=1}^l [b''_j X_2^{2j-1} + 2(-1)^\alpha (2j-1) b'_j X_2^{2j-2} + (2j-1)(2j-2) b_j X_2^{2j-3}] \right) \mathbf{E}_1 \\ &+ \frac{1}{2} \left(r'' + \sum_{i=1}^k [a''_i X_2^{2i} + 2(-1)^\alpha 2i a'_i X_2^{2i-1} + 2i(2i-1) a_i X_2^{2i-2}] \right) \mathbf{E}_2 . \end{aligned} \quad (44)$$

The variation of (43) is straight forward

$$\begin{aligned} \frac{\partial^2 \delta \tilde{\chi}}{\partial \xi_\alpha^2} &= \frac{1}{2} \left(\delta r'' + \sum_{i=1}^k [\delta a''_i X_2^{2i} + 2(-1)^\alpha 2i \delta a'_i X_2^{2i-1} + 2i(2i-1) \delta a_i X_2^{2i-2}] \right) \mathbf{E}_1 \\ &+ \frac{1}{2} \left(\sum_{j=1}^l [\delta b''_j X_2^{2j-1} + 2(-1)^\alpha (2j-1) \delta b'_j X_2^{2j-2} + (2j-1)(2j-2) \delta b_j X_2^{2j-3}] \right) \mathbf{E}_2 . \end{aligned} \quad (45)$$

The square of the stretch thus takes the form

$$\begin{aligned} \rho_\alpha^2 = & \frac{1}{2} \left(r' + \sum_{i=1}^k [a'_i X_2^{2i} + (-1)^\alpha 2i a_i X_2^{2i-1}] \right)^2 \\ & + \frac{1}{2} \left(\sum_{j=1}^l [b'_j X_2^{2j-1} + (-1)^\alpha (2j-1) b_j X_2^{2j-2}] \right)^2. \end{aligned} \quad (46)$$

The curvature of the α -fiber is

$$\begin{aligned} \frac{\partial \vartheta_\alpha}{\partial \xi_\alpha} = & -\frac{\sqrt{2}}{4\rho_\alpha^2} \left(\sum_{j=1}^l [b'_j X_2^{2j-1} + (-1)^\alpha (2j-1) b_j X_2^{2j-2}] \right) \times \\ & \times \left(r'' + \sum_{i=1}^k [a''_i X_2^{2i} + 2(-1)^\alpha 2i a'_i X_2^{2i-1} + 2i(2i-1) a_i X_2^{2i-2}] \right) \\ & + \frac{\sqrt{2}}{4\rho_\alpha^2} \left(r' + \sum_{i=1}^k [a'_i X_2^{2i} + (-1)^\alpha 2i a_i X_2^{2i-1}] \right) \times \\ & \times \left(\sum_{j=1}^l [b''_j X_2^{2j-1} + 2(-1)^\alpha (2j-1) b'_j X_2^{2j-2} + (2j-1)(2j-2) b_j X_2^{2j-3}] \right). \end{aligned} \quad (47)$$

With the reduced kinematics, we can rewrite the internal virtual work

as

$$\begin{aligned}
\delta W^{\text{int}} &= - \int_0^L \int_{-H}^H \sum_{\alpha=1}^2 \left\{ \frac{\partial \delta \chi}{\partial \xi_\alpha} \cdot (p_\alpha^1 \mathbf{e}_1 + p_\alpha^2 \mathbf{e}_2) + \frac{\partial^2 \delta \chi}{\partial \xi_\alpha^2} \cdot (m_\alpha^1 \mathbf{e}_1 + m_\alpha^2 \mathbf{e}_2) \right\} dX_2 dX_1 \\
&= - \int_0^L \int_{-H}^H \sum_{\alpha=1}^2 \left\{ \frac{\sqrt{2}}{2} \left(\delta r' + \sum_{i=1}^k [\delta a_i' X_2^{2i} + (-1)^\alpha 2i \delta a_i X_2^{2i-1}] \right) p_\alpha^1 \right. \\
&\quad + \frac{\sqrt{2}}{2} \left(\sum_{j=1}^l [\delta b_j' X_2^{2j-1} + (-1)^\alpha (2j-1) \delta b_j X_2^{2j-2}] \right) p_\alpha^2 \\
&\quad + \frac{1}{2} \left(\delta r'' + \sum_{i=1}^k [\delta a_i'' X_2^{2i} + 2(-1)^\alpha 2i \delta a_i' X_2^{2i-1} + 2i(2i-1) \delta a_i X_2^{2i-2}] \right) m_\alpha^1 \\
&\quad + \frac{1}{2} \left(\sum_{j=1}^l [\delta b_j'' X_2^{2j-1} + 2(-1)^\alpha (2j-1) \delta b_j' X_2^{2j-2} \right. \\
&\quad \left. + (2j-1)(2j-2) \delta b_j X_2^{2j-3}] \right) m_\alpha^2 \left. \right\} dX_2 dX_1 \\
&= - \int_0^L \left\{ \delta r' n^{(1)} + \delta r'' n^{(2)} + \sum_{i=1}^k (\delta a_i f_i^{(0)} + \delta a_i' f_i^{(1)} + \delta a_i'' f_i^{(2)}) \right. \\
&\quad \left. + \sum_{j=1}^l (\delta b_j k_j^{(0)} + \delta b_j' k_j^{(1)} + \delta b_j'' k_j^{(2)}) \right\} dX_1 .
\end{aligned} \tag{48}$$

with the following generalized forces

$$n^{(1)} = \int_{-H}^H \sum_{\alpha=1}^2 \frac{\sqrt{2}}{2} p_\alpha^1 dX_2, \quad n^{(2)} = \int_{-H}^H \sum_{\alpha=1}^2 \frac{1}{2} m_\alpha^1 dX_2 \tag{49}$$

and

$$\begin{aligned}
f_i^{(0)} &= \int_{-H}^H \sum_{\alpha=1}^2 [\sqrt{2}(-1)^\alpha i X_2^{2i-1} p_\alpha^1 + i(2i-1) X_2^{2i-2} m_\alpha^1] dX_2 \\
f_i^{(1)} &= \int_{-H}^H \sum_{\alpha=1}^2 \left[\frac{\sqrt{2}}{2} X_2^{2i} p_\alpha^1 + (-1)^\alpha 2i X_2^{2i-1} m_\alpha^1 \right] dX_2 \\
f_i^{(2)} &= \int_{-H}^H \sum_{\alpha=1}^2 \frac{1}{2} X_2^{2i} m_\alpha^1 dX_2
\end{aligned} \tag{50}$$

and

$$\begin{aligned}
k_j^{(0)} &= \int_{-H}^H \sum_{\alpha=1}^2 \left[\frac{\sqrt{2}}{2} (-1)^\alpha (2j-1) X_2^{2j-2} p_\alpha^2 + (2j-1)(2j-2) X_2^{2j-3} m_\alpha^2 \right] dX_2 \\
k_j^{(1)} &= \int_{-H}^H \sum_{\alpha=1}^2 \left[\frac{\sqrt{2}}{2} X_2^{2j-1} p_\alpha^2 + (-1)^\alpha (2j-1) X_2^{2j-2} m_\alpha^2 \right] dX_2 \\
k_j^{(2)} &= \int_{-H}^H \sum_{\alpha=1}^2 \frac{1}{2} X_2^{2j-1} m_\alpha^2 dX_2 .
\end{aligned} \tag{51}$$

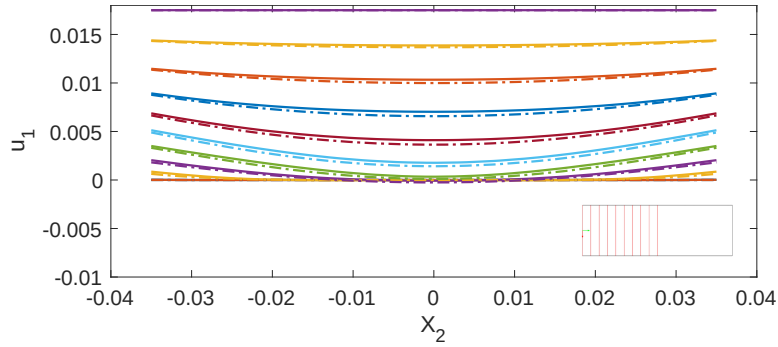


Figure 7: Longitudinal displacement u_1 in the highlighted red vertical segments. The solid lines stand for the 2D model, the dotted-dashed ones for the 1D model.

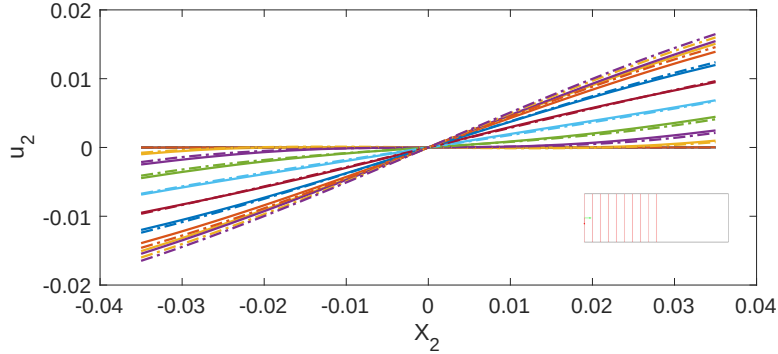


Figure 8: Transversal displacement u_2 in the highlighted red vertical segments. The solid lines stand for the 2D model, the dotted-dashed ones for the 1D model.

To illustrate the goodness of the kinematical assumptions, we performed a numerical simulation of a bias extension test using both formulations, namely the bi-dimensional and the reduced 1D. The test was conducted in a static regime on a rectangular sample with one short edge fixed and applying a uniform displacement at the opposite edge in the long-side direction with an amplitude which is half of the short edge. The k -index has been taken equal to 3, while the l -index has been set to 4. Besides, the integration

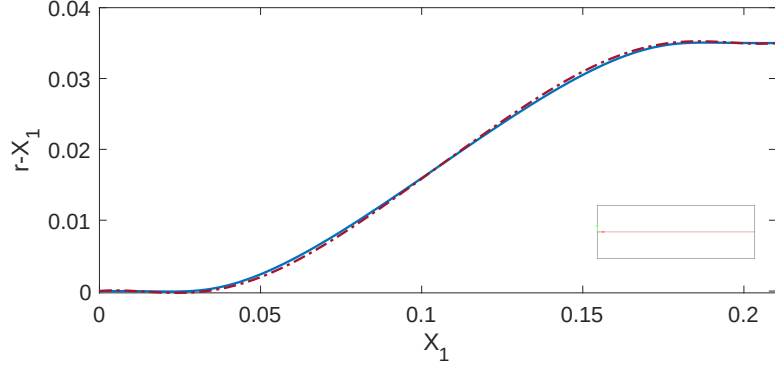


Figure 9: Longitudinal displacement u_1 in the highlighted red line. The solid line stands for the 2D model, the dotted-dashed one for the 1D model.

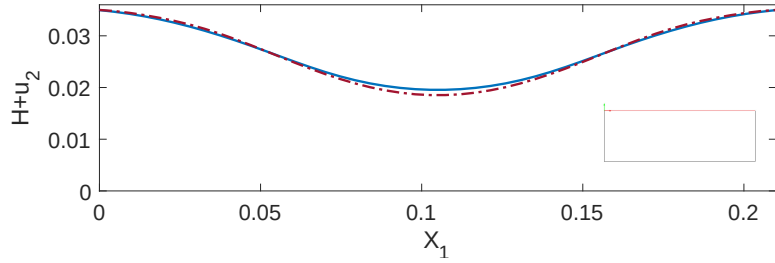


Figure 10: Outer deformed shape of the sample, i.e., χ_2 placement component in the highlighted red line. The solid line stands for the 2D model, the dotted-dashed one for the 1D model.

over the variable X_2 has been made numerically with the Gauss–Legendre quadrature using 5 points. The sample has side lengths of 0.21×0.07 m, stretching stiffness $k_e = 5.17 \times 10^5$ N/m, and bending stiffness $k_b = 0.1103$ N m. Figures 7, 8, 9, and 10 show a comparison between the two models considered in the test.

In order to derive the equation of motion of the pantographic generalized 1D continuum model also the kinetic energy must be reduced to a 1D functional. Therefore, starting from the assumed velocity field

$$\dot{\chi}(X_1, X_2, t) = \left[\dot{r}(X_1, t) + \sum_{i=1}^k \dot{a}_i(X_1, t) X_2^{2i} \right] \mathbf{e}_1 + \sum_{j=1}^l \dot{b}_j(X_1, t) X_2^{2j-1} \mathbf{e}_2 \quad (52)$$

and denoting with a dot the time-derivative, the kinetic energy takes the form:

$$K_E(\dot{\chi}) = \int_{-H}^H \int_0^L \frac{1}{2} \varrho_A \left[\left(\dot{r} + \sum_{i=1}^k \dot{a}_i X_2^{2i} \right)^2 + \left(\sum_{j=1}^l \dot{b}_j X_2^{2j-1} \right)^2 \right] dX_1 dX_2 \quad (53)$$

and after some algebraic manipulations, it becomes

$$K_E(\dot{\mathbf{X}}) = \int_{-H}^H \int_0^L \frac{1}{2} \varrho_A \left(\dot{r}^2 + 2\dot{r} \sum_{i=1}^k \dot{a}_i X_2^{2i} + \sum_{i=1}^k \sum_{j=1}^k \dot{a}_i \dot{a}_j X_2^{2(i+j)} + \sum_{i=1}^l \sum_{j=1}^l \dot{b}_i \dot{b}_j X_2^{2(i+j-1)} \right) dX_1 dX_2 \quad (54)$$

Eventually, after the integration over the X_2 variable, we obtain

$$K_E(\dot{\mathbf{X}}) = \int_0^L \varrho_A \left(H\dot{r}^2 + 2\dot{r} \sum_{i=1}^k \frac{H^{2i+1}}{2i+1} \dot{a}_i + \sum_{i=1}^k \sum_{j=1}^k \frac{H^{2(i+j)+1}}{2(i+j)+1} \dot{a}_i \dot{a}_j + \sum_{i=1}^l \sum_{j=1}^l \frac{H^{2(i+j)-1}}{2(i+j)-1} \dot{b}_i \dot{b}_j \right) dX_1 \quad (55)$$

In accordance with the principle of least action, the virtual work of the inertial actions can be deduced from the kinetic energy as

$$\begin{aligned} \delta W^{\text{ine}} = & - \int_0^L \varrho_A \left[2H\dot{r}\delta r + 2 \sum_{i=1}^k \frac{H^{2i+1}}{2i+1} (\dot{r}\delta a_i + \ddot{a}_i\delta r) \right. \\ & + \sum_{i=1}^k \sum_{j=1}^k \frac{H^{2(i+j)+1}}{2(i+j)+1} (\ddot{a}_i\delta a_j + \ddot{a}_j\delta a_i) \\ & \left. + \sum_{i=1}^l \sum_{j=1}^l \frac{H^{2(i+j)-1}}{2(i+j)-1} (\ddot{b}_i\delta b_j + \ddot{b}_j\delta b_i) \right] dX_1 \quad (56) \end{aligned}$$

5 Results of parametric numerical studies

In this section, we show the results obtained by performing numerical simulations based on the reduced 1D continuum model shortly described in the previous section.

To corroborate the hypotheses made to build the 1D model, it has been used to solve a test problem and results obtained have been compared to the ones given by the lattice beam model (see Fig. 11). In Fig. 11, some current configurations of the pantographic sheet in given time instants are provided for the two models. In order to compare the responses of the two models, we reconstructed the profile of the pantographic strip from the 1D model using the Eq. (37). The considered boundary conditions consist of an imposed displacement parallel to \mathbf{E}_1 and shaped with the signal $e = e_1$ on the left short edge, while on the right side, the same component is fixed. The components in \mathbf{E}_2 -direction are instead kept free on both sides. The input data of the lattice beam model are the same mentioned in the sect. 2. The

parameters used for the 1D model are: $k_e = 3.53 \times 10^4$ N/m; $k_b = 2.95 \times 10^{-3}$ N m; $\varrho_A = 0.263$ kg/m².

Finally, we can say that the results obtained show a very good agreement. Besides, it must be stressed that while for the lattice model the computational time was about four *hours*, for the continuum model only about four *minutes* were needed.

5.1 Axisymmetric non-linear waves induced by a class of imposed displacements to sheet short side

As announced, the three-step reduction process made feasible a parametric study of the axisymmetric non-linear waves along the \mathbf{E}_1 direction of long pantographic sheets induced by imposed displacements at one short end of the sheet.

The imposed displacement is assumed to be axisymmetric and the algorithm based on the 1D model described in the previous section can produce axisymmetric solutions only. The performed numerical simulations are characterized by a longitudinal excitation. In particular, the boundary points of the left edge are excited in \mathbf{E}_1 -direction with $e(t)$ and can move freely in \mathbf{E}_2 -direction. The points of the right edge are blocked in \mathbf{E}_1 -direction but can move freely in \mathbf{E}_2 -direction.

In order to analyze the wave propagation stemmed from the considered excitations, we introduced the centers of the distribution of the squared displacement in the transverse direction (\mathbf{E}_2) on the free long edges defines as

$$X_1^{Gt}(t) = \frac{\int_0^L X_1 [u_2(X_1, H)]^2 dX_1}{\int_0^L [u_2(X_1, H)]^2 dX_1} \quad (57)$$

and of the squared longitudinal displacement (in \mathbf{E}_1 direction) on the axis of the pantographic sheet

$$X_1^{Gl}(t) = \frac{\int_0^L X_1 [u_1(X_1, 0)]^2 dX_1}{\int_0^L [u_1(X_1, 0)]^2 dX_1} \quad (58)$$

where u_1 and u_2 are the components of the displacement in the basis $\{\mathbf{E}_1, \mathbf{E}_2\}$. With these two quantities, we have a rough idea of how the perturbation advances in the medium.

Similarly, introducing the variances for the squared transverse displacement

$$\sigma_{Gt}^2(t) = \frac{\int_0^L (X_1 - X_1^{Gt})^2 [u_2(X_1, H)]^2 dX_1}{\int_0^L [u_2(X_1, H)]^2 dX_1} \quad (59)$$

and the squared longitudinal displacement

$$\sigma_{Gl}^2(t) = \frac{\int_0^L (X_1 - X_1^{Gl})^2 [u_1(X_1, 0)]^2 dX_1}{\int_0^L [u_1(X_1, 0)]^2 dX_1}, \quad (60)$$

it is possible to deduce some features about the dispersive properties of the considered material.

Therefore, in Figs. 12 and 13, these overall quantities of the nonlinear wave propagation are displayed for the excitation $e = e_1$ varying e_0 and s_1 , respectively. We recall that these two parameters define, in the given order, the space and time amplitude of the excitation. From these pictures, it appears that the propagation velocities are different in the two examined paths, being the longitudinal propagation slower. Besides, the nonlinear behavior of the wave is most apparent in this last propagation.

In Figs. 14, 15, 17, 18, 20, and 21, we report the centers and the variances of the perturbations for the excitation $e = e_2$ varying e_0 and s_1 and changing n from 1 to 3. In all these pictures, we can see that the behavior of the propagation is particularly complex, and its features, namely the velocity and the variance, do not change monotonically with the parameters e_0 and s_1 , in some cases, making it difficult to predict them.

Figs. 16, 19, and 22 represent a typical process of propagation for the excitation $e = e_2$ and for n equal to 1, 2, and 3, respectively.

Finally, the case of point excitation is also performed (see [32] for more details). The boundary conditions are applied on the top and bottom left corner of the pantographic sheet. These points are excited by $e(t) = e_2$ with $n = 2$ in \mathbf{E}_2 -direction, the left and right edge points of the sheet are blocked in \mathbf{E}_1 -direction but can move freely in \mathbf{E}_2 -direction. Since the excitation is axisymmetric, it is possible to simulate this ulterior case with the newly introduced 1D continuum model. Figure 23 shows some current configurations obtained with the 1D reduced model in this case with point excitation.

We remark that the computing time in all these numerical simulations was about four minutes, as in the case of the test problem.

6 Conclusions and motivations for future investigations

A 1D continuum model endowed with a micro-structure suitable for describing the wave motion in a slender planar pantographic sheet, has been introduced. A number of parametric analyses of wave propagation originated by excitations applied to one end of the body have been done. The time needed to perform each one of the numerical simulations resulted to be of about four minutes. It is dramatically shorter than the one needed to perform analogous computations by means of both the lattice model and the 2D continuum model described in Sect. 3. The great saving of computing time did allow us to get remarkable information about the considered phenomenon. The results show that some non-linear waves propagates in a way suggesting that some solitary waves may arise in such a waveguide. This strongly motivates further studies in both theoretical and experimental

directions. To this aim, a generalization of the mathematical results presented in [12, 37, 44, 48, 65–67] seems necessary to give a solid ground and a logical motivation to the numerical results obtained. On the other hand, as the 1D model allows for easy and fast computation, it can help to design an experimental set-up which can prove that in pantographic sheets with sufficiently perfect pivots, waves having bounded support can propagate without relevant dispersion and attenuation for relatively long times.

References

- [1] B. E. Abali, C.-C. Wu, and W. H. Müller. An energy-based method to determine material constants in nonlinear rheology with applications. *Continuum Mechanics and Thermodynamics*, 28(5):1221–1246, 2016.
- [2] A. Aghaei, N. Bochud, G. Rosi, and S. Naili. Wave propagation across a functionally graded interphase between soft and hard solids: Insight from a dynamic surface elasticity model. *Journal of the Mechanics and Physics of Solids*, 151:104380, 2021.
- [3] J.-J. Alibert, P. Seppecher, and F. dell’Isola. Truss modular beams with deformation energy depending on higher displacement gradient. *Mathematics and Mechanics of Solids*, 8(1):51–73, 2003.
- [4] M. Arnold and O. Brüls. Convergence of the generalized- α scheme for constrained mechanical systems. *Multibody System Dynamics*, 18(2):185–202, 2007.
- [5] E. Barchiesi, F. dell’Isola, and F. Hild. On the validation of homogenized modeling for bi-pantographic metamaterials via digital image correlation. *International Journal of Solids and Structures*, 208:49–62, 2021.
- [6] E. Barchiesi, F. dell’Isola, F. Hild, and P. Seppecher. Two-dimensional continua capable of large elastic extension in two independent directions: Asymptotic homogenization, numerical simulations and experimental evidence. *Mechanics Research Communications*, 103:103466, 2020.
- [7] E. Barchiesi, S. R. Eugster, F. dell’Isola, and F. Hild. Large in-plane elastic deformations of bi-pantographic fabrics: asymptotic homogenization and experimental validation. *Mathematics and Mechanics of Solids*, 25(3):739–767, 2020.
- [8] E. Barchiesi, J. Harsch, G. Ganzosch, and S. Eugster. Discrete versus homogenized continuum modeling in finite deformation bias extension test of bi-pantographic fabrics. *Continuum Mechanics and Thermodynamics*, pages 1–14, 2020.

- [9] E. Barchiesi, M. Laudato, and F. Di Cosmo. Wave dispersion in non-linear pantographic beams. *Mechanics Research Communications*, 94:128–132, 2018.
- [10] E. Barchiesi, A. Misra, L. Placidi, and E. Turco. Granular micromechanics-based identification of isotropic strain gradient parameters for elastic geometrically nonlinear deformations. *ZAMM-Zeitschrift für Angewandte Mathematik und Mechanik*, 101(11):e202100059, 2021.
- [11] E. Barchiesi, M. Spagnuolo, and L. Placidi. Mechanical metamaterials: a state of the art. *Mathematics and Mechanics of Solids*, 24(1):212–234, 2019.
- [12] V. Y. Belashov and S. V. Vladimirov. *Solitary Waves in Dispersive Complex Media: Theory · Simulation · Applications*. Springer, 2005.
- [13] A. Berezovski, M. E. Yildizdag, and D. Scerrato. On the wave dispersion in microstructured solids. *Continuum Mechanics and Thermodynamics*, 32(3):569–588, 2020.
- [14] A. M. Bersani, F. dell’Isola, and P. Seppecher. Lagrange multipliers in infinite dimensional spaces, examples of application. *Encyclopedia of Continuum Mechanics*, pages 1425–1432, 2020.
- [15] A. Cazzani, M. Malagù, E. Turco, and F. Stochino. Constitutive models for strongly curved beams in the frame of isogeometric analysis. *Mathematics and Mechanics of Solids*, 21(2):182–209, 2016.
- [16] A. Cazzani, F. Stochino, and E. Turco. An analytical assessment of finite element and isogeometric analyses of the whole spectrum of Timoshenko beams. *ZAMM-Zeitschrift für Angewandte Mathematik und Mechanik*, 96(10):1220–1244, 2016.
- [17] A. Ciallella. Research perspective on multiphysics and multiscale materials: a paradigmatic case. *Continuum Mechanics and Thermodynamics*, 32(3):527–539, 2020.
- [18] A. Ciallella, D. Pasquali, M. Gołaszewski, F. D’Annibale, and I. Giorgio. A rate-independent internal friction to describe the hysteretic behavior of pantographic structures under cyclic loads. *Mechanics Research Communications*, 116:103761, 2021.
- [19] M. Cuomo, F. dell’Isola, and L. Greco. Simplified analysis of a generalized bias test for fabrics with two families of inextensible fibres. *Zeitschrift für angewandte Mathematik und Physik*, 67(3):1–23, 2016.

- [20] M. Dai, S. Tanaka, S. Oterkus, and E. Oterkus. Static and dynamic mechanical behaviors of cracked mindlin plates in ordinary state-based peridynamic framework. *Acta Mechanica*, pages 1–18, 2022.
- [21] M. De Angelo, L. Placidi, N. Nejadi Sadeghi, and A. Misra. Non-standard Timoshenko beam model for chiral metamaterial: identification of stiffness parameters. *Mechanics Research Communications*, 103:103462, 2020.
- [22] M. De Angelo, M. Spagnuolo, F. D’Annibale, et al. The macroscopic behavior of pantographic sheets depends mainly on their microstructure: experimental evidence and qualitative analysis of damage in metallic specimens. *Continuum Mechanics and Thermodynamics*, 31(4):1181–1203, 2019.
- [23] F. dell’Isola, I. Giorgio, and U. Andreaus. Elastic pantographic 2D lattices: a numerical analysis on the static response and wave propagation. *Proceedings of the Estonian Academy of Sciences*, 64(3):219, 2015.
- [24] F. dell’Isola, I. Giorgio, M. Pawlikowski, and N. L. Rizzi. Large deformations of planar extensible beams and pantographic lattices: heuristic homogenization, experimental and numerical examples of equilibrium. *Proceedings of the Royal Society of London A: Mathematical, Physical and Engineering Sciences*, 472(2185), 2016.
- [25] F. dell’Isola, T. Lekszycki, M. Pawlikowski, R. Grygoruk, and L. Greco. Designing a light fabric metamaterial being highly macroscopically tough under directional extension: first experimental evidence. *Zeitschrift für angewandte Mathematik und Physik*, 66(6):3473–3498, 2015.
- [26] F. dell’Isola, P. Seppecher, J.-J. Alibert, et al. Pantographic metamaterials: an example of mathematically driven design and of its technological challenges. *Continuum Mechanics and Thermodynamics*, 31(4):851–884, 2019.
- [27] F. dell’Isola, P. Seppecher, M. Spagnuolo, et al. Advances in pantographic structures: design, manufacturing, models, experiments and image analyses. *Continuum Mechanics and Thermodynamics*, 31(4):1231–1282, 2019.
- [28] F. dell’Isola, M. Spagnuolo, E. Barchiesi, I. Giorgio, and P. Seppecher. Pantographic metamaterial: a (not so) particular case. In D. J. Steigmann and F. dell’Isola, editors, *Discrete and Continuum Models for Complex Metamaterials*, pages 103–138. Cambridge University Press, 2020.

- [29] V. A. Eremeyev, F. S. Alzahrani, A. Cazzani, T. Hayat, E. Turco, V. Konopińska-Zmysłowska, et al. On existence and uniqueness of weak solutions for linear pantographic beam lattices models. *Continuum Mechanics and Thermodynamics*, 31(6):1843–1861, 2019.
- [30] V. A. Eremeyev, G. Rosi, and S. Naili. Transverse surface waves on a cylindrical surface with coating. *International Journal of Engineering Science*, 147:103188, 2020.
- [31] V. A. Eremeyev and E. Turco. Enriched buckling for beam-lattice metamaterials. *Mechanics Research Communications*, 103:103458, 2020.
- [32] S. R. Eugster. Numerical analysis of nonlinear wave propagation in a pantographic sheet. *Mathematics and Mechanics of Complex Systems*, 9(3):293–310, 2021.
- [33] G. Falsone and G. La Valle. A homogenized theory for functionally graded Euler–Bernoulli and Timoshenko beams. *Acta Mechanica*, 230(10):3511–3523, 2019.
- [34] R. Fedele. Simultaneous assessment of mechanical properties and boundary conditions based on digital image correlation. *Experimental Mechanics*, 55(1):139–153, 2015.
- [35] R. Fedele, A. Ciani, L. Galantucci, M. Bettuzzi, and L. Andena. A regularized, pyramidal multi-grid approach to global 3D-volume digital image correlation based on X-ray micro-tomography. *Fundamenta Informaticae*, 125(3-4):361–376, 2013.
- [36] Y. K. Galadima, W. Xia, E. Oterkus, and S. Oterkus. A computational homogenization framework for non-ordinary state-based peridynamics. *Engineering with Computers*, pages 1–27, 2022.
- [37] S. Gavriluk and K.-M. Shyue. Singular solutions of the bbm equation: analytical and numerical study. *Nonlinearity*, 35(1):388, 2021.
- [38] I. Giorgio. Numerical identification procedure between a micro-Cauchy model and a macro-second gradient model for planar pantographic structures. *Zeitschrift für angewandte Mathematik und Physik*, 67(4):95:1–17, 2016.
- [39] I. Giorgio. Lattice shells composed of two families of curved Kirchhoff rods: an archetypal example, topology optimization of a cycloidal metamaterial. *Continuum Mechanics and Thermodynamics*, 33(4):1063–1082, 2021.
- [40] L. Greco. An iso-parametric G^1 -conforming finite element for the nonlinear analysis of Kirchhoff rod. Part I: the 2D case. *Continuum Mechanics and Thermodynamics*, 32(5):1473–1496, 2020.

- [41] L. Greco, M. Cuomo, L. Contrafatto, and S. Gazzo. An efficient blended mixed B-spline formulation for removing membrane locking in plane curved Kirchhoff rods. *Computer Methods in Applied Mechanics and Engineering*, 324:476–511, 2017.
- [42] L. Greco, A. Scrofani, and M. Cuomo. A non-linear symmetric G1-conforming bézier finite element formulation for the analysis of Kirchhoff beam assemblies. *Computer Methods in Applied Mechanics and Engineering*, 387:114176, 2021.
- [43] J. Harsch and S. R. Eugster. Finite element analysis of planar nonlinear classical beam theories. In B. E. Abali and I. Giorgio, editors, *Developments and Novel Approaches in Nonlinear Solid Body Mechanics*, pages 123–157. Springer International Publishing, 2020.
- [44] A. T. Il’ichev and A. Y. Semenov. Stability of solitary waves in dispersive media described by a fifth-order evolution equation. *Theoretical and Computational Fluid Dynamics*, 3(6):307–326, 1992.
- [45] A. Javili, R. Morasata, E. Oterkus, and S. Oterkus. Peridynamics review. *Mathematics and Mechanics of Solids*, 24(11):3714–3739, 2019.
- [46] G. La Valle and S. Massoumi. A new deformation measure for micropolar plates subjected to in-plane loads. *Continuum Mechanics and Thermodynamics*, 34(1):243–257, 2022.
- [47] M. Laudato and A. Ciallella. Perspectives in generalized continua. In *Developments and Novel Approaches in Biomechanics and Metamaterials*, pages 1–13. Springer, 2020.
- [48] O. Le Métayer, S. Gavrilyuk, and S. Hank. A numerical scheme for the Green–Naghdi model. *Journal of Computational Physics*, 229(6):2034–2045, 2010.
- [49] F. Maurin, F. Greco, and W. Desmet. Isogeometric analysis for nonlinear planar pantographic lattice: discrete and continuum models. *Continuum Mechanics and Thermodynamics*, 31(4):1051–1064, 2019.
- [50] T. Merzouki, H. M. S. Ahmed, A. Bessaim, M. Haboussi, R. Dimitri, and F. Tornabene. Bending analysis of functionally graded porous nanocomposite beams based on a non-local strain gradient theory. *Mathematics and Mechanics of Solids*, 27(1):66–92, 2022.
- [51] A. Misra and N. Nejadi Sadeghi. Longitudinal and transverse elastic waves in 1D granular materials modeled as micromorphic continua. *Wave Motion*, 90:175–195, 2019.

- [52] A. Misra, N. Nejadi Sadeghi, M. De Angelo, and L. Placidi. Chiral metamaterial predicted by granular micromechanics: verified with 1D example synthesized using additive manufacturing. *Continuum Mechanics and Thermodynamics*, 32(5):1497–1513, 2020.
- [53] M. H. Müser, W. B. Dapp, R. Bugnicourt, et al. Meeting the contact-mechanics challenge. *Tribology Letters*, 65(4):1–18, 2017.
- [54] N. Nejadi Sadeghi and A. Misra. Role of higher-order inertia in modulating elastic wave dispersion in materials with granular microstructure. *International Journal of Mechanical Sciences*, 185:105867, 2020.
- [55] N. Nejadi Sadeghi and A. Misra. On the statics and dynamics of granular-microstructured rods with higher order effects. *Mathematics and Mechanics of Solids*, 26(12):1815–1837, 2021.
- [56] J. Niiranen, V. Balabanov, J. Kiendl, and S. Hosseini. Variational formulations, model comparisons and numerical methods for Euler–Bernoulli micro- and nano-beam models. *Mathematics and Mechanics of Solids*, 24(1):312–335, 2019.
- [57] G. Piccardo, G. Ranzi, and A. Luongo. A complete dynamic approach to the generalized beam theory cross-section analysis including extension and shear modes. *Mathematics and Mechanics of Solids*, 19(8):900–924, 2014.
- [58] A. A. Pisano and P. Fuschi. Closed form solution for a nonlocal elastic bar in tension. *International journal of Solids and Structures*, 40(1):13–23, 2003.
- [59] L. Placidi, U. Andreaus, A. Della Corte, and T. Lekszycki. Gedanken experiments for the determination of two-dimensional linear second gradient elasticity coefficients. *Zeitschrift für angewandte Mathematik und Physik*, 66(6):3699–3725, 2015.
- [60] L. Placidi, U. Andreaus, and I. Giorgio. Identification of two-dimensional pantographic structure via a linear D4 orthotropic second gradient elastic model. *Journal of Engineering Mathematics*, 103(1):1–21, 2017.
- [61] L. Placidi, E. Barchiesi, E. Turco, and N. L. Rizzi. A review on 2D models for the description of pantographic fabrics. *Zeitschrift für angewandte Mathematik und Physik*, 67(5):121, 2016.
- [62] L. Placidi, M. G. El Sherbiny, and P. Baragatti. Experimental investigation for the existence of frequency band gap in a microstructure model. *Mathematics and Mechanics of Complex Systems*, 2021.

- [63] V. L. Popov et al. *Contact mechanics and friction*. Springer, 2010.
- [64] M. K. Ravari, M. Kadkhodaei, M. Badrossamay, and R. Rezaei. Numerical investigation on mechanical properties of cellular lattice structures fabricated by fused deposition modeling. *International Journal of Mechanical Sciences*, 88:154–161, 2014.
- [65] H. Reda, N. Karathanasopoulos, K. Elnady, J.-F. Ganghoffer, and H. Lakiss. The role of anisotropy on the static and wave propagation characteristics of two-dimensional architected materials under finite strains. *Materials & Design*, 147:134–145, 2018.
- [66] H. Reda, N. Karathanasopoulos, Y. Rahali, J.-F. Ganghoffer, and H. Lakiss. Influence of first to second gradient coupling energy terms on the wave propagation of three-dimensional non-centrosymmetric architected materials. *International Journal of Engineering Science*, 128:151–164, 2018.
- [67] M. Remoissenet. *Waves called solitons: concepts and experiments*. Springer Science & Business Media, 2013.
- [68] G. Rosi, N. Auffray, and C. Combescure. On the failure of classic elasticity in predicting elastic wave propagation in gyroid lattices for very long wavelengths. *Symmetry*, 12(8):1243, 2020.
- [69] P. Seppecher, J.-J. Alibert, and F. dell’Isola. Linear elastic trusses leading to continua with exotic mechanical interactions. In *Journal of Physics: Conference Series*, volume 319, page 012018. IOP Publishing, 2011.
- [70] S. Sessa, N. Vaiana, M. Paradiso, and L. Rosati. An inverse identification strategy for the mechanical parameters of a phenomenological hysteretic constitutive model. *Mechanical Systems and Signal Processing*, 139:106622, 2020.
- [71] N. Shahrubudin, T. C. Lee, and R. Ramlan. An overview on 3D printing technology: Technological, materials, and applications. *Procedia Manufacturing*, 35:1286–1296, 2019.
- [72] B. L. Sharma and V. A. Eremeyev. Wave transmission across surface interfaces in lattice structures. *International Journal of Engineering Science*, 145:103173, 2019.
- [73] N. Shekarchizadeh, M. Laudato, L. Manzari, B. E. Abali, I. Giorgio, and A. M. Bersani. Parameter identification of a second-gradient model for the description of pantographic structures in dynamic regime. *Zeitschrift für angewandte Mathematik und Physik*, 72(6):1–24, 2021.

- [74] Y. Solyaev and S. Lurie. Electric field, strain and inertia gradient effects on anti-plane wave propagation in piezoelectric materials. *Journal of Sound and Vibration*, 494:115898, 2021.
- [75] Y. Solyaev, S. Lurie, and A. Ustenko. Numerical modeling of a composite auxetic metamaterials using micro-dilatation theory. *Continuum Mechanics and Thermodynamics*, 31(4):1099–1107, 2019.
- [76] M. Spagnuolo and A. M. Cazzani. Contact interactions in complex fibrous metamaterials. *Continuum Mechanics and Thermodynamics*, 33(4):1873–1889, 2021.
- [77] M. Spagnuolo, M. E. Yildizdag, U. Andreaus, and A. M. Cazzani. Are higher-gradient models also capable of predicting mechanical behavior in the case of wide-knit pantographic structures? *Mathematics and Mechanics of Solids*, 26(1):18–29, 2021.
- [78] M. Spagnuolo, M. E. Yildizdag, X. Pinelli, A. Cazzani, and F. Hild. Out-of-plane deformation reduction via inelastic hinges in fibrous metamaterials and simplified damage approach. *Mathematics and Mechanics of Solids*, 27(6):1011–1031, 2022.
- [79] D. Steigmann et al. A two-dimensional gradient-elasticity theory for woven fabrics. *Journal of Elasticity*, 118(1):113–125, 2015.
- [80] D. J. Steigmann and A. C. Pipkin. Equilibrium of elastic nets. *Philosophical Transactions of the Royal Society of London. Series A: Physical and Engineering Sciences*, 335(1639):419–454, 1991.
- [81] G. Taig, G. Ranzi, and F. D’Annibale. An unconstrained dynamic approach for the generalised beam theory. *Continuum Mechanics and Thermodynamics*, 27(4):879–904, 2015.
- [82] F. Tornabene, M. Viscoti, R. Dimitri, and J. N. Reddy. Higher order theories for the vibration study of doubly-curved anisotropic shells with a variable thickness and isogeometric mapped geometry. *Composite Structures*, 267:113829, 2021.
- [83] L. V. Tran and J. Niiranen. A geometrically nonlinear Euler–Bernoulli beam model within strain gradient elasticity with isogeometric analysis and lattice structure applications. *Mathematics and Mechanics of Complex Systems*, 8(4):345–371, 2020.
- [84] E. Turco. How the properties of pantographic elementary lattices determine the properties of pantographic metamaterials. In B. E. Abali, H. Altenbach, F. dell’Isola, V. A. Eremeyev, and A. Öchsner, editors, *New Achievements in Continuum Mechanics and Thermodynamics: A*

Tribute to Wolfgang H. Müller, pages 489–506. Springer International Publishing, 2019.

- [85] E. Turco and E. Barchiesi. Kinematically triggered nonlinear vibrations of Hencky-type pantographic sheets. *Mathematics and Mechanics of Complex Systems*, 9(3):311–335, 2022.
- [86] E. Turco, M. Golaszewski, I. Giorgio, and F. D’Annibale. Pantographic lattices with non-orthogonal fibres: experiments and their numerical simulations. *Composites Part B: Engineering*, 118:1–14, 2017.
- [87] E. Turco, A. Misra, M. Pawlikowski, F. dell’Isola, and F. Hild. Enhanced Piola–Hencky discrete models for pantographic sheets with pivots without deformation energy: numerics and experiments. *International Journal of Solids and Structures*, 147:94–109, 2018.
- [88] Z. Vangelatos, G. X. Gu, and C. P. Grigoropoulos. Architected metamaterials with tailored 3D buckling mechanisms at the microscale. *Extreme Mechanics Letters*, 33:100580, 2019.
- [89] Z. Vangelatos, V. Melissinaki, M. Farsari, K. Komvopoulos, and C. Grigoropoulos. Intertwined microlattices greatly enhance the performance of mechanical metamaterials. *Mathematics and Mechanics of Solids*, 24(8):2636–2648, 2019.
- [90] H. Yang, B. E. Abali, D. Timofeev, and W. H. Müller. Determination of metamaterial parameters by means of a homogenization approach based on asymptotic analysis. *Continuum mechanics and thermodynamics*, 32(5):1251–1270, 2020.
- [91] M. E. Yildizdag, M. Demirtas, and A. Ergin. Multipatch discontinuous Galerkin isogeometric analysis of composite laminates. *Continuum Mechanics and Thermodynamics*, 32(3):607–620, 2020.
- [92] M. Zeidi and C. I. Kim. Mechanics of fiber composites with fibers resistant to extension and flexure. *Mathematics and Mechanics of Solids*, 24(1):3–17, 2019.

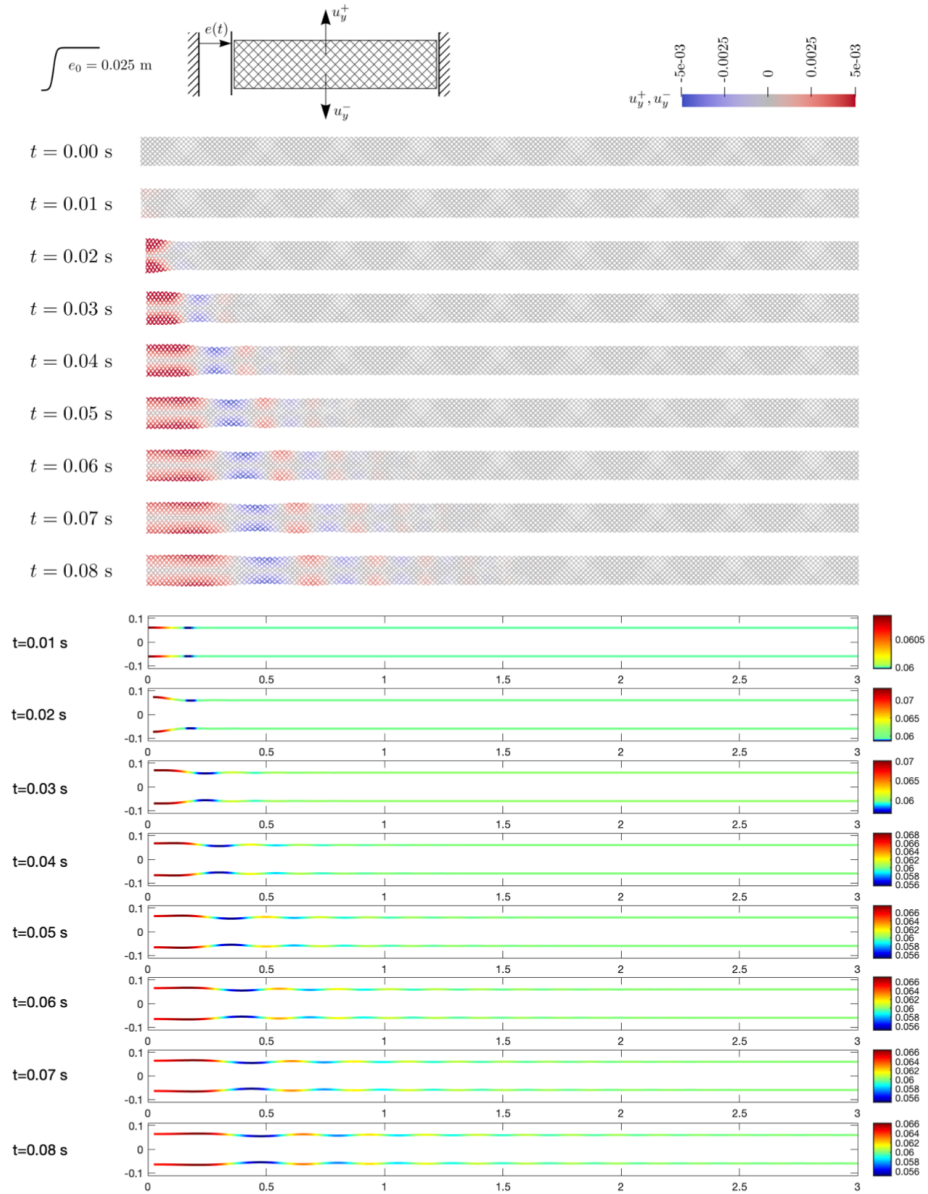


Figure 11: Comparison between the planar beam lattice model (top) and the 1D reduced continuum model (bottom). Excitation with $e = e_1$, $e_0 = 0.025$ m and $s_1 = 0.01625$ s. Colors indicate the transverse displacement.

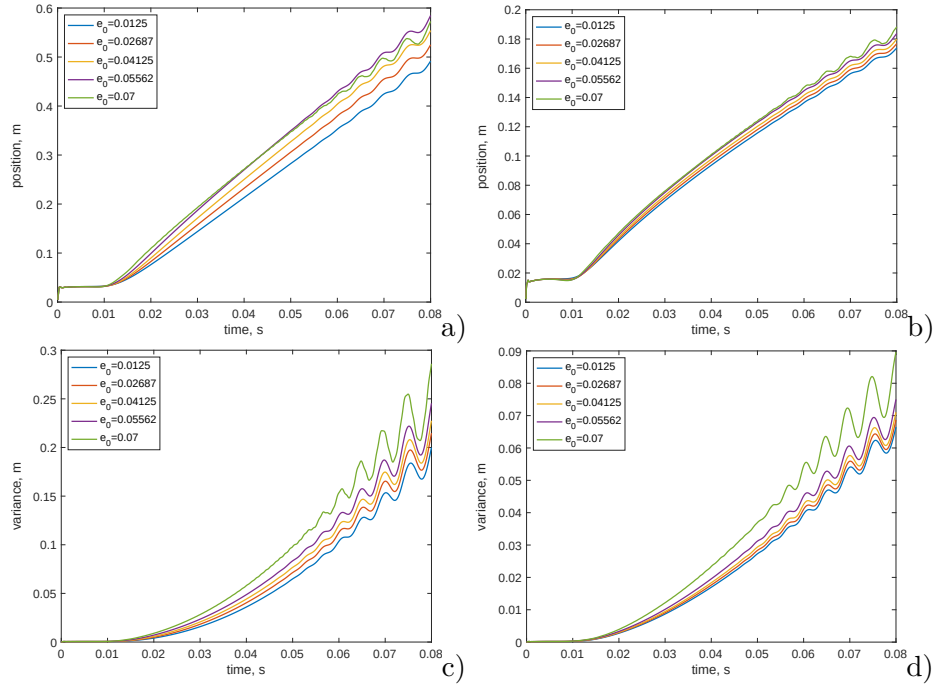


Figure 12: Excitation with $e = e_1$, $s_1 = 0.01$ s and varying e_0 : X_1^{Gt} a); X_1^{Gl} b); σ_{Gt}^2 c); σ_{Gl}^2 d).

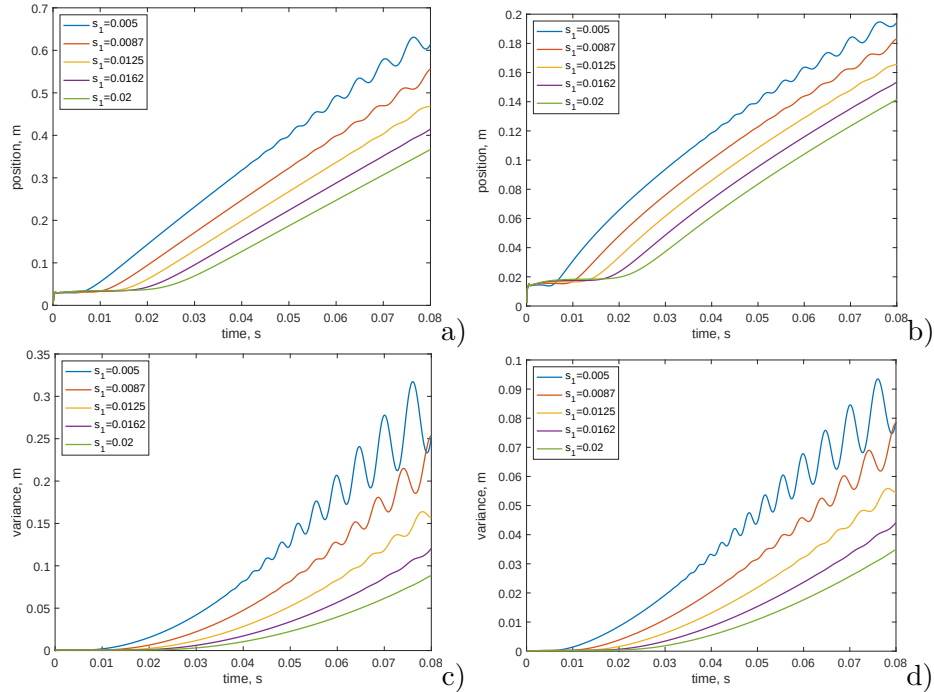


Figure 13: Excitation with $e = e_1$, $e_0 = 0.025$ m and varying s_1 : X_1^{Gt} a); X_1^{Gl} b); σ_{Gt}^2 c); σ_{Gl}^2 d).

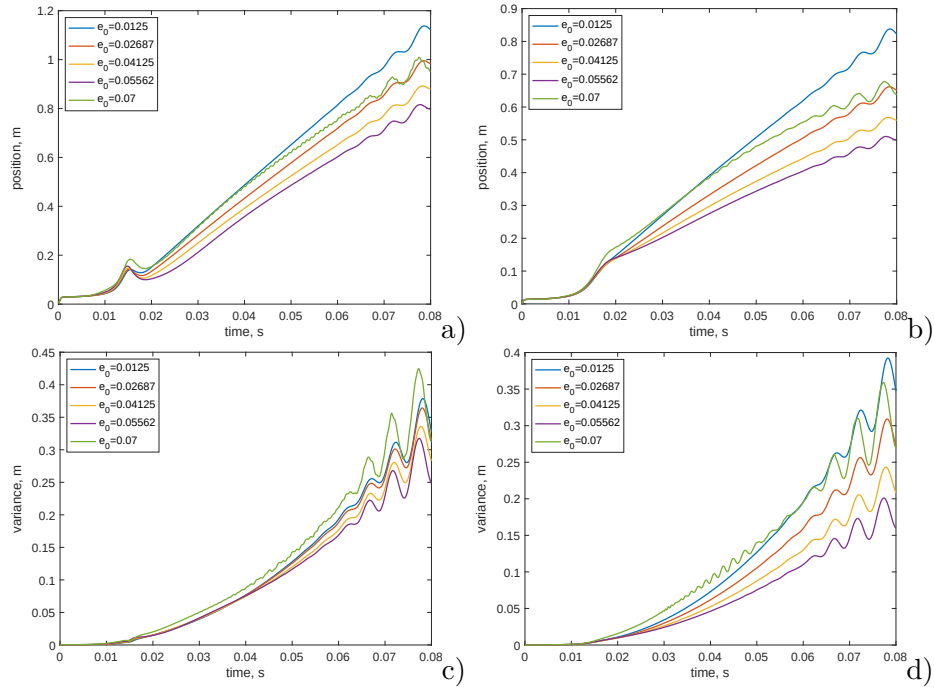


Figure 14: Excitation with $e = e_2$, $n = 1$, $s_1 = 0.01$ s and varying e_0 : X_1^{Gt} a); X_1^{Gl} b); σ_{Gt}^2 c); σ_{Gl}^2 d).

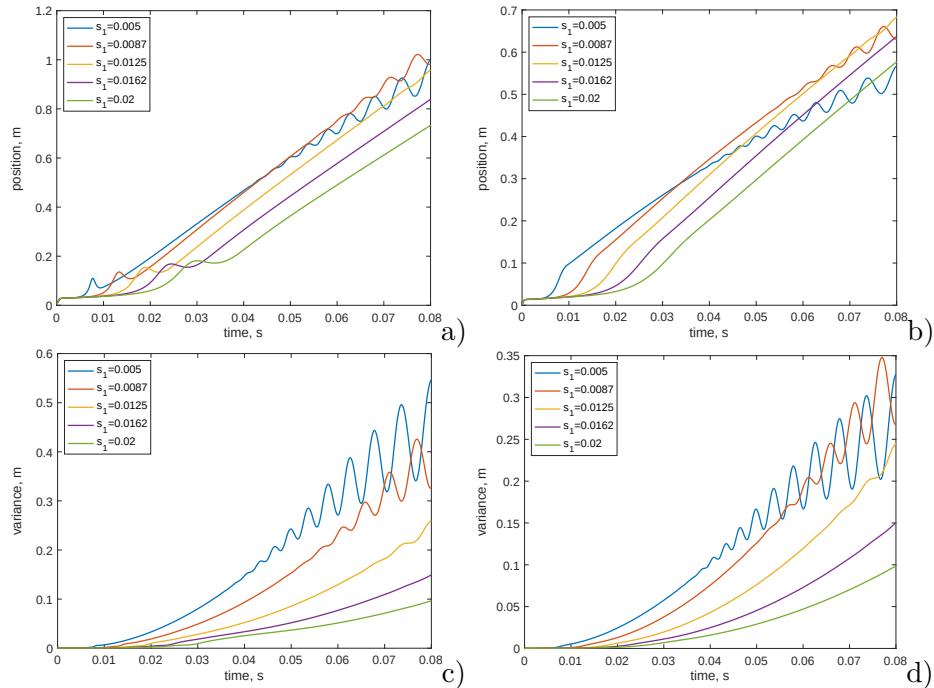


Figure 15: Excitation with $e = e_2$, $n = 1$, $e_0 = 0.025$ m and varying s_1 : X_1^{Gt} a); X_1^{Gl} b); σ_{Gt}^2 c); σ_{Gl}^2 d).

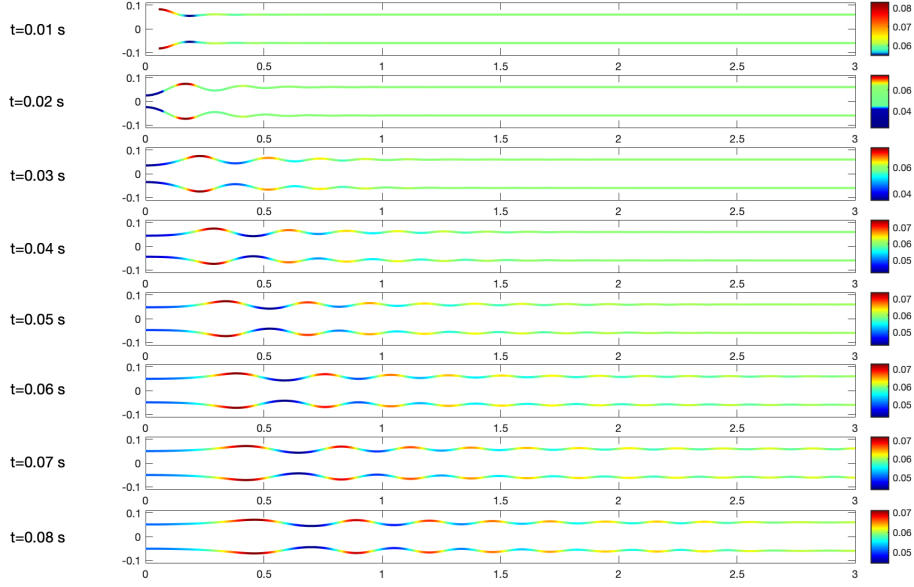


Figure 16: Excitation with $e = e_2$, $n = 1$, $e_0 = 0.055625$ m and $s_1 = 0.01$ s.

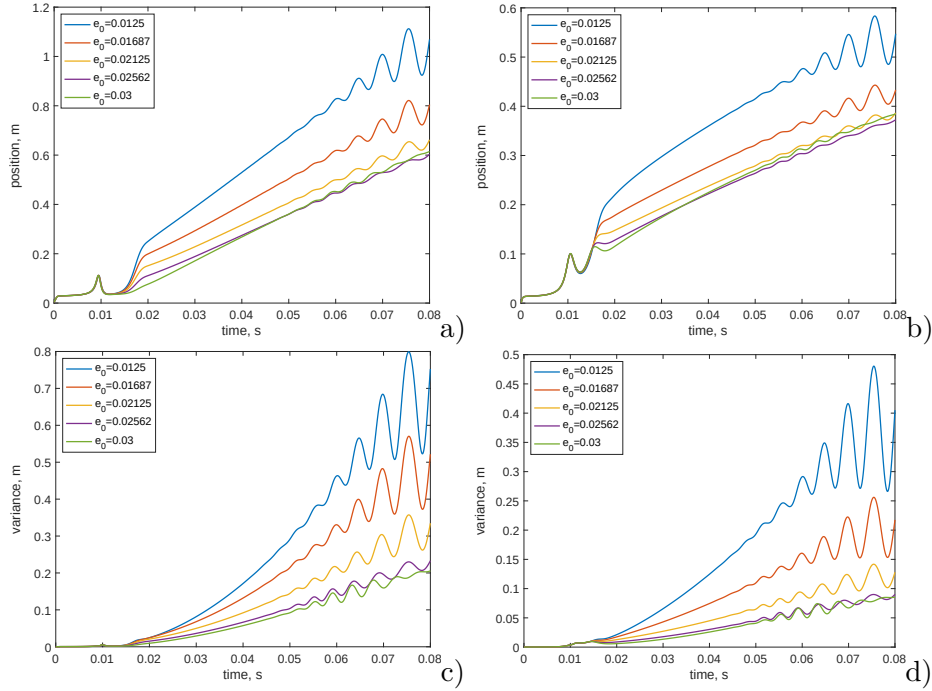


Figure 17: Excitation with $e = e_2$, $n = 2$, $s_1 = 0.01$ s and varying e_0 : X_1^{Gt} a); X_1^{Gt} b); σ_{Gt}^2 c); σ_{Gt}^2 d).

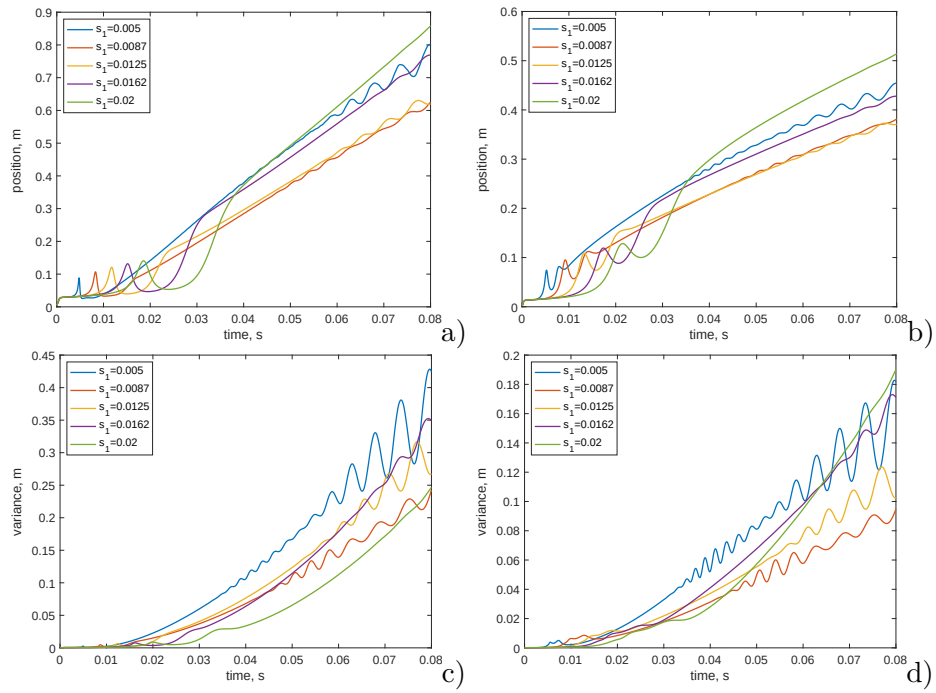


Figure 18: Excitation with $e = e_2$, $n = 2$, $e_0 = 0.025$ m and varying s_1 : X_1^{Gt} a); X_1^{Gt} b); σ_{Gt}^2 c); σ_{Gt}^2 d).

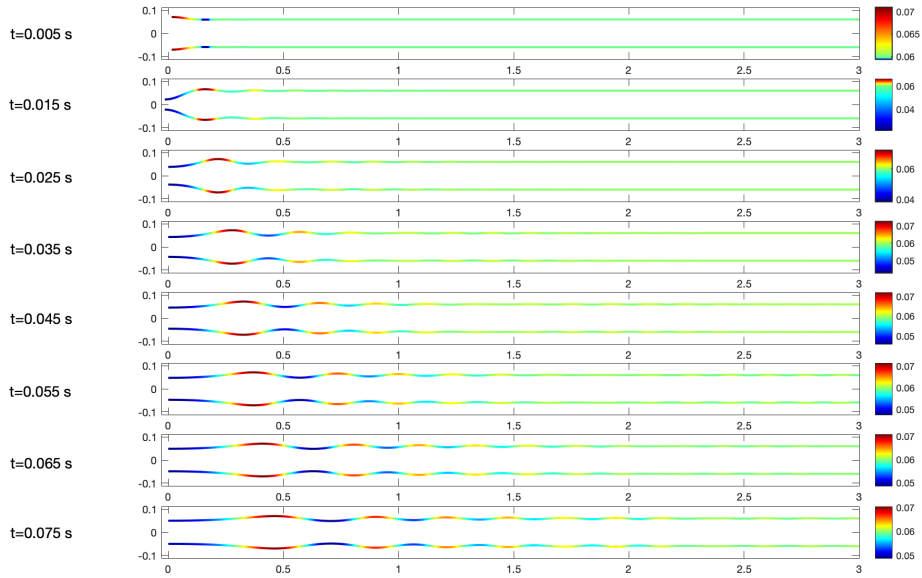


Figure 19: Excitation with $e = e_2$, $n = 2$, $e_0 = 0.03$ m and $s_1 = 0.01$ s.

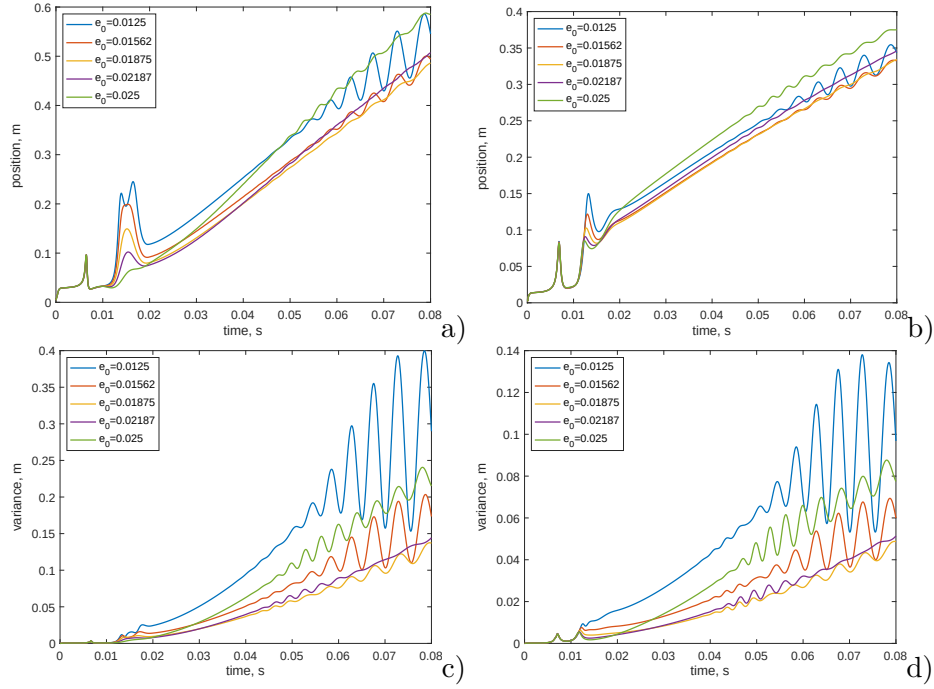


Figure 20: Excitation with $e = e_2$, $n = 3$, $s_1 = 0.01$ s and varying e_0 : X_1^{Gt} a); X_1^{Gl} b); σ_{Gt}^2 c); σ_{Gl}^2 d).

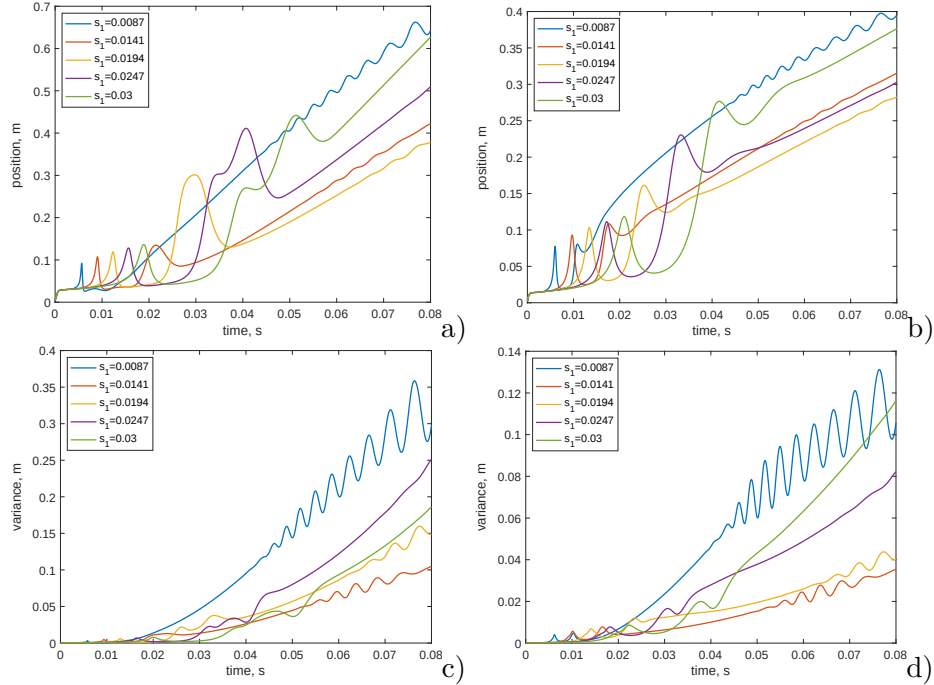


Figure 21: Excitation with $e = e_2$, $n = 3$, $e_0 = 0.025$ m and varying s_1 : X_1^{Gt} a); X_1^{Gl} b); σ_{Gt}^2 c); σ_{Gl}^2 d).

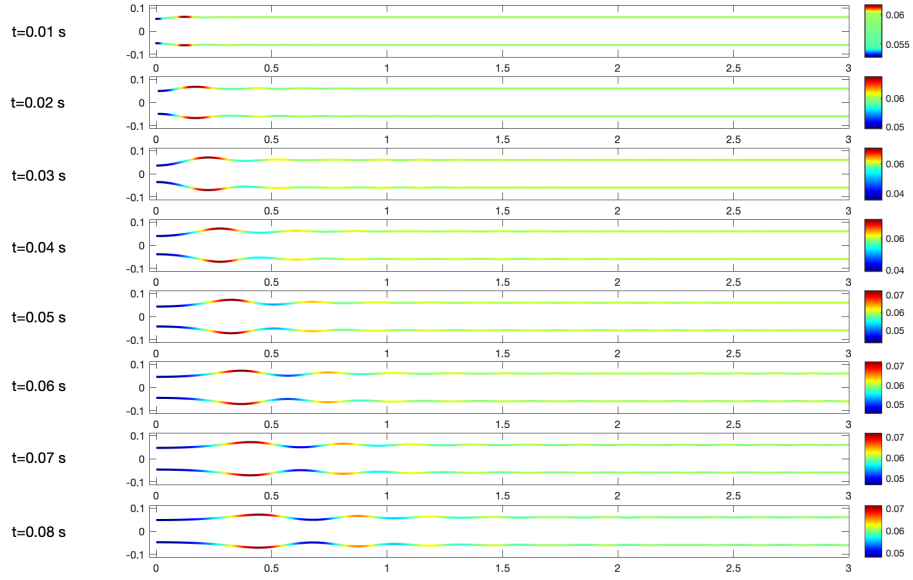


Figure 22: Excitation with $e = e_2$, $n = 3$, $e_0 = 0.025$ m and $s_1 = 0.014063$ s.

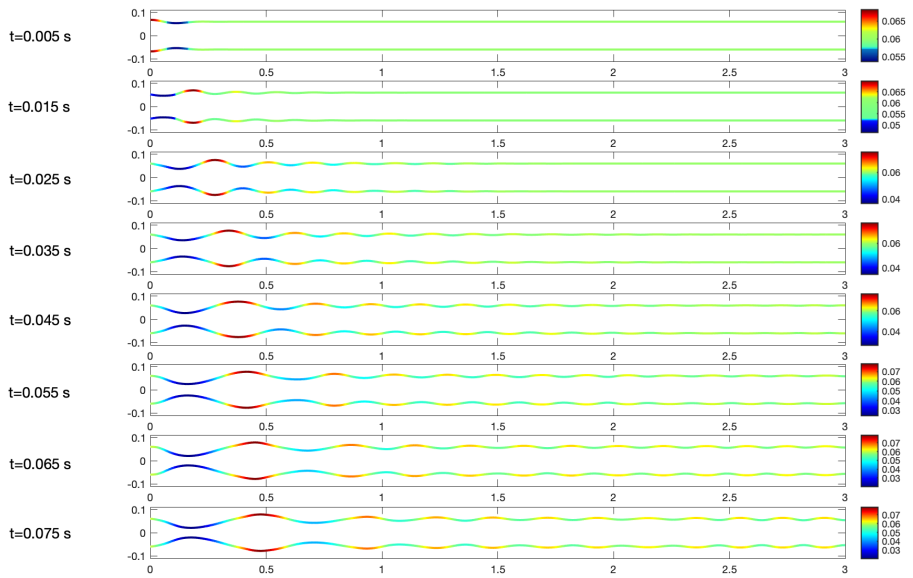


Figure 23: Point excitation with $e = e_2$, $n = 2$, $e_0 = 0.075$ m and $s_1 = 0.01$ s.